The magnitude of the snow-sourced reactive nitrogen flux to the boundary layer in the Uintah Basin, Utah, USA

Maria Zatko[1], Joseph Erbland[2,3], Joel Savarino[2,3], Lei Geng[1,a], Lauren Easley[4], Andrew Schauer[5], Timothy Bates[7], Patricia K. Quinn[6], Bonnie Light[8], David Morison[8,b], Hans D. Osthoff[9], Seth Lyman[10], William Neff[11], Bin Yuan[11,12], Becky Alexander[1]

[1]Department of Atmospheric Sciences, University of Washington, Seattle, 98195, USA

[2]Université Grenoble Alpes, LGGE, 38000 Grenoble, France

[3]CNRS, LGGE, 38000 Grenoble, France

[4]Department of Chemistry, University of Washington, Seattle, Washington, 98195, USA

[5]Earth and Space Sciences, University of Washington, Seattle, Washington, 98195, USA

[6]Pacific Marine Environmental Laboratory, National Oceanic and Atmospheric Administration, Seattle, Washington, 98115, USA

[7]Joint Institute for the Study of the Atmosphere and Oceans, University of Washington, Seattle, Washington, 98195, USA

[8]Polar Science Center, Applied Physics Laboratory, University of Washington, Seattle, Washington, 98195, USA

[9]Department of Chemistry, University of Calgary, 2500 University Drive NW, Calgary, AB T2N 1N4, Canada

[10]Bingham Entrepreneurship and Energy Research Center, Utah State University, 320 Aggie Boulevard, Vernal, Utah, 84078, USA

[11]Cooperative Institute for Research in the Environmental Sciences, University of Colorado, Boulder, Colorado, 80309, USA

[12]Chemical Sciences Division, Earth System Research Laboratory, National Oceanic and Atmospheric Administration, Boulder, Colorado, 80305, USA

[a]Now at Université Grenoble Alpes, LGGE, 38000 Grenoble, France, CNRS, LGGE, 38000 Grenoble, France

[b]Now at Department of Physics and Astronomy, University of Utah, Salt Lake City, Utah, 84112, USA

Correspondence to Becky Alexander (beckya@uw.edu)

Abstract

Reactive nitrogen (N_r=NO, NO_2, HONO) and volatile organic carbon emissions from oil and gas extraction activities play a major role in wintertime ground-level ozone exceedance events of up to 140 ppb in the Uintah Basin in eastern Utah. Such events occur only when the ground is snow covered, due to the impacts of snow on the stability and depth of the boundary layer and ultraviolet actinic flux at the surface. Recycling of reactive nitrogen from the photolysis of snow nitrate has been observed in polar and mid-latitude snow, but snow-sourced reactive nitrogen fluxes in mid-latitude regions have not yet been quantified in the field. Here we present vertical profiles of snow nitrate concentration and nitrogen isotopes ($\delta^{15}N$) collected during the Uintah Basin Winter Ozone Study 2014 (UBWOS 2014), along with observations of insoluble light-absorbing impurities, radiation equivalent mean ice grain radii, and snow density that determine snow optical properties. We use the snow optical properties and nitrate concentrations to calculate ultraviolet actinic flux in snow and the production of N_r from the photolysis of snow nitrate. The observed $\delta^{15}N(NO_3^-)$ is used to constrain modeled fractional loss of snow nitrate in a snow chemistry column model, and thus the source of N_r to the overlying boundary layer. Snow-surface $\delta^{15}N(NO_3^-)$ measurements range from -5‰ to 10‰ and suggest that the local nitrate burden in the Uintah Basin is dominated by primary emissions from anthropogenic sources, except during fresh snowfall events, where remote NO_x sources from beyond the basin are dominant. Modeled daily-averaged snow-sourced N_r fluxes range from 5.6-71x10^7 molec cm^{-2} s^{-1} over the course of the field campaign, with a maximum noon-time value of 3.1x10^9 molec cm^{-2} s^{-1}. The top-down emission estimate of primary, anthropogenic NO_x in the Uintah and Duchesne counties is

at least 300 times higher than the estimated snow NO_x emissions presented in this study. Our results suggest that snow-sourced reactive nitrogen fluxes are minor contributors to the N_r boundary layer budget in the highly-polluted Uintah Basin boundary layer during winter 2014.

1. Introduction

Ozone (O_3) has adverse respiratory effects, is an effective greenhouse gas [*UNEP*, 2011], and, through formation of the hydroxyl radical, influences the oxidizing capacity of the atmosphere [*Thompson,* 1992]. O_3 precursors include volatile organic compounds (VOCs) emitted from vegetation, biomass burning, and fossil fuel combustion [*Guenther et al*., 1995, *Warneke et al*., 2014] and nitrogen oxides (NO_x=NO+NO_2) emitted from fossil fuel combustion, biomass burning, soil microbial activity, lightning, and photochemical reactions in snow [*Delmas et al*., 1997, *Grannas et al*., 2007, *Logan et al*., 1983]. Maximum boundary layer O_3 concentrations are typically observed during the summer in major cities, where O_3 precursors are abundant and when conditions favor efficient O_3 production (high ultraviolet (UV) radiation) and air stagnation. High O_3 concentrations in the boundary layer exceeding 100 ppbv were measured in winter 2005 in the Upper Green River Basin in rural Wyoming [*Schnell et al*., 2009], well above the current Environmental Protection Agency (EPA) National Ambient Air Quality Standard (NAAQS) 8-hour average limit of 70 ppbv. High wintertime O_3 episodes have also been observed in the Uintah Basin in rural Utah [*Martin et al*., 2011], and in both basins, these O_3 episodes only occur when the ground is snow-covered [*Oltmans et al*., 2014]. The Upper Green River Basin and the Uintah Basin are regions of major oil and gas development, and the production of oil and natural gas in the Upper Green River Basin and the Uintah Basin is expected to increase through at least 2020 [*US EIA*, 2014].

These wintertime high O_3 episodes motivated a series of field campaigns, including the Upper Green Winter O_3 Study (UGWOS 2011, UGWOS 2012) and the Uintah Basin

113 Winter O_3 Study (UBWOS 2012, UBWOS 2013, UBWOS 2014). Results from these
114 field campaigns [*Gilman et al*., 2013, *Helmig et al*., 2014, *Oltmans et al*., 2014, *Warneke*
115 *et al*., 2014, *Schnell et al*., 2009] and subsequent modeling studies [*Ahmadov et al*., 2015,
116 *Carter and Seinfeld*, 2012, *Edwards et al*., 2013, 2014, *Field et al*., 2015, *Rappengluck et*
117 *al*., 2014] reveal that emissions of NO_x and VOCs from oil and gas extraction, combined
118 with stagnant meteorological conditions, enhanced boundary layer UV radiation due to
119 the high UV albedo of snow [*Warren et al*., 2006], and reduced O_3 loss through surface
120 deposition due to snow cover [*Ahmadov et al*., 2015], trigger high boundary layer O_3
121 episodes in these basins. O_3 exceedance events occur only when the ground is snow
122 covered because snow aids in the formation and maintenance of a stable air mass and
123 reflects UV radiation upwards into the boundary layer. O_3 exceedance events end when
124 stable boundary layers are disrupted by the passage of storm fronts, which often deposit
125 snow. Modeling studies were used to determine whether O_3 formation in these regions is
126 NO_x-sensitive or VOC-sensitive, which is necessary information for the enactment of
127 effective regulations aimed to reduce boundary layer O_3 abundance. Modeling results
128 from Edwards et al. [2014] suggest that the Uintah Basin is in an O_3 formation regime on
129 the boundary between VOC-sensitive and NO_x-sensitive and modeling results from
130 Ahmadov et al. [2015] suggest that the Uintah Basin regime is VOC-sensitive. Modeling
131 results presented in Edwards et al. [2014] suggest that the dominant radical sources in the
132 Uintah Basin are carbonyl compounds (85%), with smaller inputs from HONO, O_3, and
133 nitryl chloride ($ClNO_2$) photolysis.
134

135 Atmospheric measurements in the Uintah Basin during UBWOS2012, UBWOS2013, and
136 UBWOS2014 reveal that the total reactive nitrogen abundances
137 (NO_y=NO+NO_2+HNO_3+PAN+N_2O_5+NO_3+$ClNO_2$+organic nitrates) are highest (12-24
138 ppbv) in 2013 due to persistent shallow inversion layers trigged by stagnant air masses
139 and snow cover, lowest in 2012 (4-9 ppbv) when no snow covered the ground, and in-
140 between (8-18 ppbv) in winter 2014, with the highest NO_y values generally in mid-day
141 [*Wild et al*., 2016]. In 2013, HNO_3 accounted for nearly half of total NO_y while in 2012
142 N_2O_5 and $ClNO_2$ were larger components of total NO_y compared to HNO_3 [*Wild et al*.,
143 2016]. Interestingly, atmospheric NO_x mixing ratios are similar in all three years, with
144 diurnal averages ranging from 2 ppbv during the night to 10 ppbv during the day [*Wild et*
145 *al*., 2016]. The NO_x/NO_y ratio, indicative of the rate of oxidation of reactive nitrogen,
146 was highest in 2013 and lowest in 2012, with intermediate values in 2014 [*Wild et al*.,
147 2016]. HO_2NO_2 measurements range from 0 to 2.4 ppbv in 2013 and ~0 to 0.4 ppbv in
148 2014 [*Veres et al*., 2015] and are generally positively correlated with snow nitrite
149 concentrations, suggesting that HO_2NO_2 deposition may be a source of snow nitrite
150 [*Veres et al*., 2015].
151
152 In addition to aiding in the formation and maintenance of a stable air mass with enhanced
153 UV radiation, snow may also recycle reactive nitrogen oxides (N_r = NO_x, HONO)
154 between the snow surface and the overlying atmosphere, effectively increasing the
155 atmospheric lifetime of N_r. The major sink of N_r in the atmosphere is the formation and
156 deposition of nitrate (particulate NO_3^- plus HNO_3(g)). When nitrate is deposited to snow,
157 its photolysis serves to recycle N_r to the overlying boundary layer [*Grannas et al.,* 2007,

158 *Honrath et al*., 2000]. This snow-sourced N_r can then be re-oxidized to nitrate and re-
159 deposited to the snow surface. The recycling of nitrogen between the snow surface and
160 boundary layer can occur many times, resulting in the continuous recycling of N_r during
161 sunlit conditions.
162
163 The photolysis of nitrate occurs in the liquid-like region (LLR) in or on ice grains
164 [*Domine et al*., 2013] in the top snow layer where UV radiation is present, which is
165 known as the snow photic zone. Snow nitrate photolyzes at wavelengths (λ)=290-345 nm
166 to produce aqueous-phase nitrogen dioxide (NO_2) or nitrite (NO_2^-) according to E1 and
167 E2 [*Grannas et al*., 2007, *Mack and Bolton*, 1999, *Meusinger et al*., 2014].
168
169 $NO_3^-(aq) + h\nu(+H^+) \rightarrow NO_2(aq) + OH(aq)$, E1
170 $NO_3^-(aq) + h\nu \rightarrow NO_2^-(aq) + O(^3P)(aq)$, E2
171
172 The measured quantum yields (ϕ) for E1 range from 0.003-0.6 molec photon^{-1} at 253 K
173 [*Chu and Anastasio*, 2003, *Meusinger et al*., 2014, *Zhu et al*., 2010], and is likely
174 influenced by the location of nitrate within ice grains. The NO_2 produced in E1 quickly
175 evaporates due to its low solubility and can be transported to the overlying atmosphere.
176 The nitrite produced in E2 is rapidly photolyzed at longer wavelengths (λ=290-390 nm)
177 (E3).
178
179 $NO_2^-(aq) + h\nu(+H^+, aq) \rightarrow NO(aq) + OH(aq)$, E3
180

Nitrite can also react with OH or H^+ in the LLR to produce aqueous-phase NO_2 and HONO [*Grannas et al*., 2007]:

$NO_2^-(aq) + OH(aq) \rightarrow NO_2(aq) + OH^-(aq)$, E4

$NO_2^-(aq) + H^+(aq) \rightarrow HONO(aq)$, E5

HONO can rapidly photolyze in the LLR to produce aqueous-phase NO and OH [*Anastasio and Chu*, 2009]; due to its short lifetime the aqueous-phase OH remains in the LLR, but the aqueous-phase NO can be transferred to the gas phase and ultimately be released into the boundary layer. Under acidic conditions ($pk_a < 2.8$), aqueous-phase HONO can also be transferred to the gas phase (HONO (aq) $\leftrightarrow$ HONO (g)) [*Anastasio and Chu*, 2009] and released into the boundary layer, where it can photolyze to produce gas-phase NO and OH [*Zhou et al*., 2001].

Nitrate nitrogen isotopes ($\delta^{15}N(NO_3^-)$) in the air and snow can provide useful information about snow photochemistry, specifically, the degree of photolysis-driven recycling and loss of nitrate from the snow. Nitrogen isotope ratios are expressed as $\delta^{15}N$, where $\delta = R_{sample}/R_{reference} - 1$, $R = {}^{15}N/{}^{14}N$, and N_2-air is the reference material. Nitrate photolysis in snow is a mass-dependent process and is associated with a large fractionation constant (ε) of -47.9‰ at wavelengths shorter than 320 nm [*Berhanu et al*., 2014]. Nitrate photolysis provides the boundary layer with a source of N_r that is highly depleted in ^{15}N, leaving highly enriched $\delta^{15}N(NO_3^-)$ deeper in the snow. Snow-sourced nitrate that is redeposited to the snow surface is lighter than the remaining nitrate in the snow, leading to $\delta^{15}N(NO_3^-$

204) values that become more enriched with increasing depth within the snow photic zone.
205 $\delta^{15}N(NO_3^-)$ values in the atmosphere are also influenced by the relative importance of
206 different NO_x sources [see *Felix and Elliott,* 2014 for a summary]. For example, the
207 atmospheric $\delta^{15}N$ signature from anthropogenic NO_x sources, such as combustion of
208 fossil fuels, range from -19.0‰ to 25.0‰ [*Felix et al.,* 2012, *Walters et al*., 2015]. The
209 $\delta^{15}N$ signature from soil microbial activity is generally lower than that of anthropogenic
210 activity and ranges from -50‰ to -20‰ [*Felix and Elliott*, 2014]. Observations of
211 atmospheric $\delta^{15}N(NO_3^-)$ in non-polluted, mid-latitude regions range from -6 to -2‰,
212 while $\delta^{15}N(NO_3^-)$ values measured in polluted regions range from 0 to 6‰ [*Morin et al*.,
213 2009]. In addition, atmospheric $\delta^{15}N(NO_3^-)$ is influenced by NO_x cycling [*Freyer et al*.,
214 1993; *Walters et al*., 2016], NO_2 oxidation [*Walters and Michalski*, 2015], and the
215 partitioning of nitrate between its gas and particulate phases [*Heaton et al*., 1997].
216
217 In this study, we investigate the importance of snow photochemistry as a source of
218 reactive nitrogen oxides to the boundary layer in the Uintah Basin using chemical,
219 isotopic, and optical measurements from the snow collected during the UBWOS 2014
220 campaign. In Section 2 we describe the field, laboratory, and modeling techniques used in
221 this study. In Section 3 we present the chemical and optical measurements made during
222 UBWOS 2014 and model-calculated fluxes of snow-sourced N_r. In Section 4 we estimate
223 the contribution of snow-sourced N_r to the N_r burden in the Uintah Basin boundary layer.
224

2. Methods

2.1. Field and Laboratory Observations

2.1.1. UBWOS 2014 Field Site Description and Meteorological Conditions

UBWOS 2014 occurred from January 17, 2014 to February 13, 2014 at the Horsepool field-intensive site (40.1°N, 109.5°W) in the Uintah Basin, roughly 35 miles south of Vernal, Utah. There are over 10,000 oil and natural gas wells in the basin connected by a series of dirt roads. The meteorological conditions were relatively constant for most of the campaign; wind speeds ranged from 1 to 3 m s^{-1} and often originated from the southwest. Sky conditions were clear, temperatures ranged from 258 to 275 K, and boundary layer heights generally ranged from 25 to 150 m. There were a few cloudy days (January 29-February 4, February 10) during the campaign and the last several days experienced temperatures above freezing. Daily maximum boundary layer O_3 mixing ratios ranged from 45 ppb to 90 ppb, and the campaign-averaged daily-maximum boundary layer O_3 mixing ratio was 61 ppb.

Snow covered the ground throughout the duration of the campaign, and ranged in depth from 10 to 30 cm, depending on how snow was redistributed by wind after deposition. The snow was deep enough to cover some of the lowest-lying vegetation, but branches from bushes were still visible. Three snow events occurred before the campaign, one event on December 4, which deposited most of the snow (19 cm), and two smaller events on December 8 and December 19, which deposited roughly 3 cm and 1 cm of snow,

248 respectively. There was a distinct crust layer roughly 4 cm below the snow surface,
249 providing evidence of surface melting between the later two snowfall events. The
250 temperature difference between the soil and the air was at least 15 K for several weeks,
251 allowing vapor to redistribute through the snow, leading to the formation of large hoar
252 crystals (radiation equivalent mean ice grain radii [*Hansen and Travis*, 1974] (r_e) > 1200
253 μm) at all depths in the snow. There was one major snow event during the campaign on
254 January 30 through January 31 that deposited roughly 5 cm of fresh snow (r_e ~ 100 μm).
255 There were two smaller snow events on February 4 and February 10. On February 4 there
256 was no measureable snow accumulation and during the early-morning hours of February
257 10 there was 2 cm of fresh snow that subsequently melted several hours after sunrise.
258 Supplementary Figure 3B summarizes daily snow accumulation before and during the
259 campaign.
260
261 **2.1.2 Snowpit Measurements and Snow Sample Preparation**
262 Twelve snowpits were dug approximately every 2 to 3 days during the campaign.
263 Snowpits were dug from the snow surface to about 1 cm above the subniveal ground and
264 ranged in depth from 9 to 24 cm. The snowpits were dug in a variety of directions
265 roughly 150 meters from the main Horsepool site, except for snowpit 5 (January 24),
266 which was dug roughly 800 meters away from Horsepool. The snowpits were dug
267 wearing clean, nitrate-free gloves using a stainless steel spatula. For each snowpit,
268 vertical profiles (1-cm depth resolution) of snow density (ρ_{snow}), temperature, and
269 radiation equivalent ice grain radii (r_e) were measured using a Taylor-LaChapelle snow
270 density kit, a dial stem thermometer, and a laminated snow grid card with 1 mm grid

271 spacing, respectively. Snow grains from each distinct snow layer were placed on the
272 snow grid card and a photograph was taken. The photographs were projected onto a
273 larger screen and the shortest dimension of each snow crystal was estimated. The shortest
274 dimension of a snow grain is the most optically important dimension [*Grenfell and*
275 *Warren*, 1999], and in this study, it is used to represent r_e. For hoar crystals, the smallest
276 dimension is the width of the crystal wall and for freshly-fallen crystals, the smallest
277 dimension is the radius of the rounded crystal. For each snowpit, approximately 1 kg of
278 snow was collected at 1-cm depth intervals and placed into 'whirl-pak' plastic bags. The
279 bags were kept covered while in the field and then immediately placed into a freezer once
280 back at the Utah State University (USU) Uintah Basin Campus in Vernal, Utah.
281 Supplementary section A shows detailed information on each snowpit.
282

283 **2.1.3. Optical Measurements**

284 The snow from each plastic bag was spooned into a clean glass beaker and melted in a
285 microwave oven at USU. The meltwater was transferred to a stainless steel funnel and
286 passed through a 0.4 μm Nuclepore filter, using an electric diaphragm vacuum pump to
287 create a partial vacuum in a volumetric flask. The Nuclepore filter collects insoluble light
288 absorbing impurities (LAI) in snow, including black carbon (BC) and non-black carbon
289 (non-BC) species, the latter of which encompass brown carbon, dust, and organics. The
290 volume of filtrate was measured, which ranged from 40 to 750 ml depending on impurity
291 content. After the Nuclepore filters dried overnight, the filters were frozen until further
292 analysis at the University of Washington (UW).
293

The absorption spectrum of each Nuclepore filter was measured using an ISSW spectrophotometer [*Grenfell et al*., 2011] in the Arctic Snow Laboratory at UW. The Nuclepore filter is placed between two integrating spheres lined with Spectralon material to create a fully diffuse medium. An Ocean Optics USB-650 spectrophotometer is used to measure the absorption spectrum in units of optical depth, $\tau(\lambda)$ (dimensionless, e.g. cm^2 cm^{-2}), from λ=350-1000 nm in 10 nm intervals. A set of standard filters containing known loadings of black carbon (Fullerene) is used to calibrate the ISSW spectrophotometer. The spectral absorption measured by the spectrophotometer for each filter is characterized by an Ångstrom exponent ($\mathring{A}$), which represents the total absorption by both BC and non-BC LAI on the filter between two visible wavelengths. $\mathring{A}$ is calculated in E7:

$$\mathring{A}(\lambda_1 \; to \; \lambda_2) = \frac{\ln\left(\frac{\tau(\lambda_1)}{\tau(\lambda_2)}\right)}{\ln\left(\frac{\lambda_2}{\lambda_1}\right)} \;, \qquad \text{E7}$$

where λ_1=450 nm and λ_2=600 nm. The λ=450-600 nm range is chosen because the ISSW spectrophotometer signal is most stable over this wavelength range. The total absorption Ångstrom exponent on each filter along with assumed Ångstrom exponents for BC ($\mathring{A}$=1) and non-BC ($\mathring{A}$=5) are used to estimate snow BC concentrations and the fraction of ultraviolet (λ=300-350 nm) absorption by non-BC material (see *Doherty et al*., 2010, *Grenfell et al*., 2011, *Zatko et al*., 2013, and *Zatko and Warren*, 2015). Triplicate measurements were performed for all samples.

Surface upwelling and downwelling irradiance was measured using a commercial spectral radiometer equipped with a photodiode array (Metcon GMBH,

317 http://www.metcon-us.com). Upwelling and downwelling UV-A and UV-B were
318 measured with Kipp and Zonen Model UV-S-AB-T radiometers. Radiometers were
319 placed at 2 m above ground (one up-facing and one down-facing) and were cleaned and
320 checked weekly to ensure that the radiometers remained directly perpendicular to the
321 ground. Detailed irradiance data is provided in the Supplemental Material.
322
323 **2.1.4. Chemical Concentration and Nitrate Isotopic Measurements**
324 In a laboratory on the USU campus in Vernal, UT, a 50 µl aliquot of snow meltwater that
325 was passed through the Nuclepore filter was used to measure ion (Cl^-, Br^-, NO_3^-, SO_4^{2-},
326 Na^+, NH_4^+, K^+, Mg^{+2}, Ca^{+2}, oxalate) concentrations using a Metrohm 761 Compact Ion
327 Chromatograph Analyzer [*Quinn et al*., 1998]. The nitrate in the remaining filtrate was
328 preconcentrated for isotopic analysis. Nitrate was preconcentrated by passing the
329 meltwater through an anion exchange resin (BioRad AG 1-X8) using an electric
330 diaphragm pump. The sample anions in the resin were eluted with 5x2 ml 1 M sodium
331 chloride (NaCl/Milli-Q water) solution into a 30 ml pre-cleaned sample bottle. This
332 method has been shown to ensure full recovery of nitrate [*Silva et al*., 2000, *Frey et al*.,
333 2009] The solution was kept frozen in the dark until analysis in the University of
334 Washington IsoLab (http://isolab.ess.washington.edu/isolab/).
335
336 The denitrifier method [*Casciotti et al*., 2002, *Kaiser et al*., 2007, *Sigman et al*., 2001]
337 was used to determine the nitrogen isotopic signature ($\delta^{15}N$) in each snow sample.
338 Denitrifying bacteria, *Pseudomonas aureofaciens,* convert nitrate to nitrous oxide (N_2O)
339 gas in anaerobic conditions [*Casciotti et al*., 2002, *Sigman et al*., 2001] and N_2O is

transported via helium gas through a heated gold tube (800°C), where it thermally decomposes into O_2 and N_2. After separation by gas chromatography, the O_2 and N_2 are run through a Thermo Finnigan™ DeltaPlus Advantage isotope ratio mass spectrometer (IRMS), equipped with a Precon and GasBench II™. The $\delta^{15}N$ values were calculated with respect to N_2 (air) via two international reference materials USGS32 ($\delta^{15}N$ =180‰) and USGS34 ($\delta^{15}N$ =-1.8‰), with IAEA ($\delta^{15}N$ =4.7‰) as a quality control standard. For many samples, the $NaCl/NO_3^-$ solution was diluted with Milli-Q water to obtain the optimal nitrate concentration (200 nmol in 2 ml) for each sample run on the IRMS. Triplicate measurements were performed for all samples. The analytical uncertainty of $\delta^{15}N(NO_3^-)$ (1σ) was 0.75‰ based on repeated measurements of the quality control standard.

Aerosol nitrate was collected throughout the campaign in 12-hour intervals. Aerosol nitrate was sampled from an inlet 13 meters above ground and drawn through a heated (283K) pipe, where it was then collected on a two-stage, multi-jet cascade impactor. The impactor tedlar films separates aerosols with diameters less than 2.5 μm from those with diameters between 2.5 to 12.5μm. The aerosols were extracted from the filters and analyzed using ion chromatography, following methods described in Quinn et al. [2000]. Gas-phase nitric acid was measured using an Acetate HR-ToF-CIMS instrument throughout the campaign with 1-minute time resolution, as described in Yuan et al. [2016].

2.2. Calculations

363

364 **2.2.1. Snow Radiative Transfer Model**

365 A 4-stream, plane-parallel radiative transfer model using the discrete ordinates method
366 with a δ-M transformation originally described in Grenfell et al. [1991] was used to
367 calculate vertical profiles of UV actinic flux in each snowpit. This model properly treats
368 layers with differing refractive indices and the 4-stream model produces albedo and
369 absorptivity results that agree to within 1% of higher-order models representative of snow
370 [*Wiscombe*, 1977], including DISORT [*Stamnes et al*., 1988]. Vertical profiles of the
371 ρ_{snow}, r_e, and LAI absorption are used to calculate vertical profiles of inherent optical
372 properties (IOPs) in snow at the wavelengths relevant for photochemistry (UV). These
373 wavelength-dependent IOPs include the bulk extinction coefficient in snow ($Kext_{tot}$) and
374 the co-albedo of single scattering ($c\varpi_{eff}$); see Zatko et al. [2013] for more details about
375 the IOP calculations. $Kext_{tot}$ and $c\varpi_{eff}$, along with observations of downwelling surface
376 UV irradiance, solar zenith angle, cloud fraction, and soil albedo (0.1) [*Markvart et al*.,
377 2003, *Matthias et al*., 2000] are used to calculate 1-cm resolution vertical profiles of UV
378 actinic flux for each snowpit, following methods described in Zatko et al. [2013]. The
379 UV actinic flux profiles are used to calculate depth-dependent photolysis rate constants
380 for nitrate photolysis in snow as described below.

381

382 **2.2.2. Snow-Sourced Reactive Nitrogen Flux Calculations**

383 The modeled vertical profiles of actinic flux and observed snow nitrate concentrations are
384 used to calculate daily-average fluxes of snow-sourced N_r from each snowpit according
385 to E8.

$$F_{Nr}(z) = \int_{\lambda_0}^{\lambda_1} \sigma_{NO_3^-}(\lambda) \cdot \phi(T,pH) \cdot I(\lambda, z) \cdot [NO_3^-](z)\, d\lambda, \quad \text{E8}$$

$F_{Nr}(z)$ is the flux of snow-sourced N_r (molec cm^{-2} s^{-1}) at 1-cm depth (z) increments in the snow, σ_{NO3}^- is the wavelength (λ)-dependent absorption cross-section for nitrate photolysis (cm^2) from Berhanu et al. [2014], ϕ is the temperature- and pH-dependent quantum yield for nitrate photolysis (ϕ, molec $photon^{-1}$) from Chu and Anastasio [2003] (4.6×10^{-3} molec $photon^{-1}$ at T=267 K), I is the depth (z)- and λ-dependent actinic flux in the snow photic zone (photons cm^{-2} s^{-1} nm^{-1}), and $[NO_3^-](z)$ is the observed nitrate concentration (ng g^{-1}) in each snow layer. E8 is integrated over the UV wavelength region (λ=298-345 nm). The snow photic zone is defined as three times the e-folding depth of UV actinic flux in snow [*Zatko et al*., 2016]. The total flux of N_r to the boundary layer, F_{Nr}, is calculated according to E9.

$$F_{Nr} = \sum_{z_0}^{z_{3e}} F_{Nr}(z) \quad \text{E9}$$

Observed surface downwelling irradiance values for a solar zenith angle of 65°, the average SZA from mid-December to mid-February, are used for calculation of $I(\lambda,z)$ in E8. Therefore the calculated F_{Nr} values represent daily-averaged F_{Nr} values. It is assumed that all N_r escapes into the boundary layer due to its low solubility.

2.2.3. Snow Photochemistry Column Model (TRANSITS)

408 The flux of snow-sourced N_r from each snowpit is also calculated using a snow
409 photochemistry column model, TRansfer of Atmospheric Nitrate Stable Isotopes To the
410 Snow (TRANSITS) model [*Erbland et al*., 2015]. TRANSITS is a multilayer, one-
411 dimensional model that simulates nitrate photochemistry in the snow and allows for
412 chemical exchange between the air and snow and calculates the isotopic composition of
413 snow nitrate. The model was originally developed to simulate snow nitrate photolysis and
414 subsequent nitrogen recycling at the air-snow interface on the East Antarctic plateau
415 (Dome C), and has been adapted to mid-latitude, shallow-snowpack conditions for this
416 study. The model has a well-mixed, atmospheric boundary layer with a height of 50 m
417 and a snow compartment containing up to 50 1-cm thick layers. In the atmosphere and in
418 each snow layer, the model solves a general mass-balance equation for nitrate
419 concentration and isotopic composition [*Erbland et al*., 2015] at each time step (1 hour).
420
421 In TRANSITS, nitrate is deposited to the snow surface via dry deposition. Nitrate dry-
422 deposition is calculated using the campaign-averaged observed boundary layer mixing
423 ratios for HNO_3 (5784 ng m^{-3}) and NO_3^- (5777 ng m^{-3}) and an assumed dry-deposition
424 velocity of 0.03 cm s^{-1}, which is similar to the dry-deposition velocity used in Edwards et
425 al. [2013, 2014] (0.02 cm s^{-1}) (see Supplementary Table 1B for nitrate dry-deposition
426 fluxes). Nitrate diffuses through the snowpack based on a diffusion coefficient that is
427 dependent on temperature, pressure, snow specific surface area, snow density, and
428 tortuosity [*Crowley et al*., 2010, *Durham et al*., 1986, *Massmann*, 1998].
429

We include only the major channel for the production of N_r from nitrate photolysis (E1) in TRANSITS. The minor channels, E2-E5, all consist of chemistry of the intermediate in nitrate photolysis, nitrite, which will photolyze or react rapidly once produced to form N_r. We assume no export of snow-sourced N_r out of the atmospheric box, which is consistent with the low wind speeds and stable boundary layer conditions observed during the campaign. In this way there is no net loss of nitrate from the snow; however, vertical redistribution of snow nitrate can occur which would result in distinctive vertical profiles of nitrate concentration and $\delta^{15}N(NO_3^-)$ in the snow column. In addition to calculating the flux of snow-sourced N_r, TRANSITS calculates vertical profiles of nitrate concentration and isotopes ($\delta^{15}N(NO_3^-)$) in the snow. To calculate $\delta^{15}N(NO_3^-)$ in the snow, the nitrate photolysis fractionation factor ($^{15}\varepsilon_{pho}$) is calculated at each time step and is dependent upon the spectral distribution of the UV irradiance at the snow surface [*Bernhau et al*., 2014, *Erbland et al*., 2015]. Calculated $^{15}\varepsilon_{pho}$ values range from -88 to -35‰ between the snowpits and are constant with snow depth.

In this study, TRANSITS is run at hourly resolution and is spun up beginning 27 days before the start of the campaign using available atmospheric chemical (boundary layer gas-phase and aerosol-phase nitrate) and meteorological data (air temperature and pressure). A constant model boundary layer height of 50 m is assumed, which is a rough estimate of daily-averaged boundary layer heights based on sodar facsimile data from NOAA. The campaign-averaged observed boundary layer total nitrate (HNO_3+ NO_3^-) mixing ratio (11.56 μg m^{-3}) was used to spin up the model. We collected and measured atmospheric $\delta^{15}N(NO_3^-)$ throughout the campaign using a high volume air sampler with

453 Nylasorb filters. However, comparison with the aerosol nitrate (NO_3^-) concentration
454 measurements from the PMEL two-stage, multi-jet cascade impactor measurements
455 revealed incomplete trapping. Since non-quantitative collection of nitrate may influence
456 the observed $\delta^{15}N(NO_3^-)$ values, the data was not used in this study. We instead use
457 surface snow $\delta^{15}N(NO_3^-)$ observations to represent atmospheric $\delta^{15}N(NO_3^-)$ (Figure 1a).
458 The TRANSITS snowpack is initialized by setting the snow height equal to 50 cm, the
459 snow photic zone to 6 cm (average photic zone depth for all snowpits), and using the
460 measured snow nitrate concentration and $\delta^{15}N(NO_3^-)$ vertical profiles from the first
461 snowpit of the campaign (January 15). The snowfall event on January 31 is simulated in
462 the model, but the other smaller events are not included. As the model evolves,
463 "snapshots" of the top 25-cm of snow are taken on days corresponding to each snowpit
464 and modeled profiles of nitrate concentration and $\delta^{15}N(NO_3^-)$ are compared to observed
465 profiles for each snowpit. Since vertical profiles of snow $\delta^{15}N(NO_3^-)$ are highly sensitive
466 to photochemical-driven redistribution of N_r in the snowpack [*Erbland et al.*, 2013,
467 2015], observed $\delta^{15}N(NO_3^-)$ provides a metric to assess model-calculated F_{Nr}.
468
469 **3. Results and Discussion**
470
471 **3.1. Observations**
472
473 **3.1.1. Nitrate Concentrations and $\delta^{15}N(NO_3^-)$ in the Surface Snow**
474 Figure 1a shows mean surface snow $\delta^{15}N(NO_3^-)$ values for each snowpit, which range
475 from -5.5 to 11.1‰. The lowest observed surface snow $\delta^{15}N(NO_3^-)$ occurred immediately

476 after the only significant fresh snowfall event on Jan. 30 – 31 (-5.5‰). All other surface
477 snow samples were over 10‰ higher (5.2 to 11.1‰).
478
479 Figure 1b shows surface snow nitrate concentration measurements for each snowpit,
480 which range from 800 to 18,000 ng g^{-1}. Similar to $\delta^{15}N(NO_3^-)$, surface-snow nitrate
481 concentrations are lowest during the snowfall event on January 30 through January 31,
482 with the exception of February 11 when the snow was rapidly melting. Similarly,
483 boundary layer gas (HNO_3) and aerosol-phase (NO_3^-) nitrate mixing ratios decrease by a
484 factor of 6 between January 30 and January 31 (Supplementary Figure 1B) compared to
485 the rest of the field campaign. In addition to the gas and aerosol phase nitrate mixing
486 ratios presented in the Supplemental Material, Veres et al. [2015] also show decreases in
487 the daily-maximum HO_2NO_2 mixing ratios on January 30 and January 31 during
488 UBWOS2014. The decrease in HO_2NO_2 mixing ratios corresponds to a sharp decrease in
489 snow nitrite concentrations (see Figure 7 in Veres et al. [2015]).
490
491
492 Generally, the surface-snow $\delta^{15}N(NO_3^-)$ values fall within the range of primary
493 anthropogenic $\delta^{15}N$ values (4-25‰) [*Felix and Elliott*, 2014, *Walters et al*., 2015].
494 During snow events the boundary layer is less stable, possibly allowing for the transport
495 of nitrate from remote sources outside the basin. In unpolluted, mid-latitude
496 environments, background atmospheric $\delta^{15}N(NO_3^-)$ ranges from -6 to -2‰ [*Morin et al*.,
497 2009]. During the major snowfall event on January 30 - 31, surface-snow $\delta^{15}N$ values are
498 ~10‰ lower compared to the rest of the campaign, suggesting that nitrate from beyond

499 the basin deposits to the snow surface. Two-day NOAA HYSPLIT back trajectories
500 [*Rolph*, 2016, *Stein et al*., 2015] show that the air mass on January 31 in the Uintah Basin
501 originated in the Pacific Ocean, which is distinctly different from the other air masses
502 that reached the Uintah Basin during UBWOS2014 (see Supplemental Material, Figures
503 4B-15B). Uintah Basin boundary layer air masses typically originated in the
504 intermountain west region and often centered over eastern Utah for several days.
505
506
507 **3.1.2. Snow Depth Profiles of Snow Optical Properties, Nitrate Concentrations, and**
508 **$\delta^{15}N(NO_3^-)$**
509 In this section and the following sections, we focus on three snowpits (January 22,
510 January 31, February 4) as being representative of the time period before, during, and
511 after the largest snow event. The other 9 snowpits will not be discussed in detail, but
512 observed and modeled vertical profiles of chemical and optical measurements for all 12
513 snowpits can be found in Supplementary section A.
514
515 Figures 2a and 2b show vertical profiles of snow optical properties from an 18-cm deep
516 snowpit dug on January 22, which represents typical profiles from the beginning of the
517 field campaign until before the first snow event. Black carbon concentrations (C_{BC}, ng g^{-1})
518 range from 3 to 100 ng g^{-1} with the highest concentrations in the top several
519 centimeters of snow. Below 3 cm snow depth, C_{BC} decreases dramatically. Figure 2b
520 shows the average absorption Ångstrom exponent ($\mathring{A}$) from λ=450-600 nm. Over this
521 wavelength range, the dominant absorber at the snow surface is non-BC material ($\mathring{A}$ is

522 nearly 5), and both BC and non-BC contribute to absorption in sub-surface snow layers
523 ($\AA$ ranges from 2 to 2.7). Although BC and non-BC material are both responsible for the
524 absorption of radiation at λ=450-600 nm, non-BC material is responsible for between
525 99.6 and 100% of UV (λ=300-350 nm) absorption at all depths in this and in all snowpits
526 measured during the field campaign. The top 3 cm of snow contains the highest
527 concentration of both BC and non-BC material; we define this layer as the "dusty layer"
528 and is represented as a brown shaded region in Figure 2.
529
530 Figures 2c and 2d show vertical profiles of snow optical properties from a 14-cm deep
531 snowpit dug on January 31. It snowed 5 cm between the afternoon of January 30 and
532 morning of January 31, and this new snow layer is evident in Figures 2c and 2d because
533 the dusty layer is now located roughly 5 cm below the snow surface. Figure 2c shows that
534 C_{BC} ranges from 5 to 100 ng g^{-1}; the maximum C_{BC} value has been buried deeper into the
535 snow. Figure 2d shows that $\AA$ is close to 1 at the snow surface, indicating that BC
536 material dominates visible absorption at the snow surface immediately following the
537 fresh snowfall event. Figures 2e and 2f show vertical profiles of snow optical properties
538 from a 24-cm deep snowpit dug on February 4, 5 days after the snow event. In this
539 snowpit, C_{BC} ranges from 4 to 100 ng g^{-1} and $\AA$ ranges from 1.7 to 3.4. Figures 2e and 2f
540 show that the original dusty layer is still located roughly 5 cm below the snow surface
541 and that a new dusty layer has formed at the snow surface.
542
543 Figures 3a-c shows observed vertical profiles of nitrate in snow from snowpits dug on
544 January 22, January 31, and February 4. Prior to the fresh snowfall event, snow nitrate

concentrations are highest at the surface (13,900 ng g^{-1}), and decrease exponentially in the top 10 cm to a low of 90 ng g^{-1} at 18 cm depth (Figure 3a). Immediately following the fresh snowfall event, the highest nitrate concentrations (12,200 ng g^{-1}) are buried below 5 cm of fresh snow within the dusty layer at 5 – 7 cm depth. The measured nitrate concentrations in the fresh snow layer range from 1,280 to 4,640 ng g^{-1}, which is up to 10 times lower than nitrate concentrations in the dusty layer (Figure 3b). Five days after the fresh snowfall event, the highest nitrate concentrations are still located roughly 7 cm below the snow surface within the dusty layer, but surface nitrate concentrations are a factor of 2 higher compared to immediately after the fresh snowfall event (Figure 3c).

Figures 3d-f shows measured snow $\delta^{15}N(NO_3^-)$ in each of the snowpits, which ranges from -5.5‰ to 13‰. In the Jan. 22 snowpit, measured $\delta^{15}N(NO_3^-)$ is highest near the top and bottom of the snowpit and lowest from 12-cm to 16-cm depth (Figure 3d). Following the fresh snowfall event on Jan. 30 – 31, snow $\delta^{15}N(NO_3^-)$ values are lightest at the snow surface and increase with depth in the fresh snow layer until the top of the dusty layer, below which they decrease to -3.5‰ (Figure 3e). Five days after the fresh snowfall event, measured $\delta^{15}N(NO_3^-)$ is most enriched in the dusty layer and at the snow surface (Figure 3f).

The last snowfall event prior to the start of the campaign occurred on December 19 and resulted in roughly 1 cm of snow accumulation (Supplementary Figure 5A). The high concentrations of LAI and nitrate in surface snow on January 22, combined with the prolonged lack of snowfall, suggest continual dry-deposition of LAI to the surface snow.

We speculate that the major source of LAI originates from truck traffic on the dirt roads in the area of the field site due to high values of $\AA$ (Figure 2). The factor of 150 and 17 decrease in nitrate and black carbon concentrations, respectively, from the surface to 18-cm depth on January 22 suggests that minimal nitrate and LAI are transported (via e.g., diffusion or meltwater transport) from upper to lower snow layers. Immediately after the snowfall event on January 31, nitrate and black carbon concentrations are 10 and 3 times lower, respectively, in the surface snow layers compared to earlier in January, because the fresh snow has lower concentrations of these species. Even just five days after the snowfall event on January 30 - 31, concentrations of nitrate and the Ångstrom exponent ($\AA$) in the snow surface layer have increased by a factor of 2, likely due to dry deposition of these species to the surface in the absence of snowfall.

The $\delta^{15}N(NO_3^-)$ profiles in snow do not immediately suggest significant photolysis-driven redistribution of nitrate in the snowpack, which would result in the lightest values at the surface, increasing exponentially with depth as observed in Antarctica [*Erbland et al*., 2013]. Prior to the first snowfall event on January 30-31, the surface dusty layer contains the highest values of measured $\delta^{15}N(NO_3^-)$, which are similar to that expected from primary emission of NO_x from anthropogenic sources [*Felix and Elliott*, 2014, *Walters et al*., 2015]. We speculate that the depleted $\delta^{15}N(NO_3^-)$ values towards the bottom of the snowpit correspond to remote-sourced atmospheric nitrate that was deposited during the large snow event (~20 cm of snow) on December 4. Emissions of microbial NO from subniveal soil could also lead to depleted $\delta^{15}N(NO_3^-)$ if this NO is oxidized to nitrate in the snowpack and deposited to the surface of snow grains before

escaping to the atmosphere. However, the depleted $\delta^{15}N(NO_3^-)$ would also likely correspond with enhanced nitrate concentrations, which is not observed (Figures 3a-c). Additionally, calculations by Zatko et al. [2013] suggest that the lifetime of NO_x against oxidation to HNO_3 in snow interstitial air is long enough so that most NO emitted from soil microbial activity would likely be transported to the atmospheric boundary layer prior to oxidation. On January 31, depleted $\delta^{15}N(NO_3^-)$ measurements at the snow surface suggest that there is deposition of nitrate from less polluted regions surrounding the basin during the snow event. The increase in surface snow $\delta^{15}N(NO_3^-)$ values after January 31 is likely due to deposition of primary-sourced nitrate from anthropogenic NO_x sources in the basin. In the following section, we examine the influence of photolysis of snow nitrate on the profiles of $\delta^{15}N(NO_3^-)$ in snow.

3.2. Calculations

3.2.1. Calculations of Snow Actinic Flux Profiles and Flux of Snow-Sourced N_r

Figure 4a-c show calculated vertical profiles of UV actinic flux normalized to surface downwelling irradiance for the three snowpits. On January 22, the normalized actinic flux ratio is nearly 4 at the snow surface because actinic flux is calculated by integrating irradiance over a sphere (surface area of $4\pi r^2$) and also because scattering in snow dominates over absorption. In Figure 4a, the actinic flux decreases to 2.9 within the top centimeter of snow due mainly to UV absorption by non-BC in the surface snow layer. The actinic flux is rapidly extinguished in the dusty layer and continues to decrease with increasing depth in the snow, reaching a value of 0.01 at 18-cm depth. The blue shaded

614 region represents the snow photic zone (top 5 cm of snow) on January 22. The snow
615 photic zones calculated in this study (4-7 cm) are much shallower compared to calculated
616 snow photic zones in polar regions (72-207 cm in Antarctica, 6-51 cm in Greenland)
617 [*Zatko et al*., 2016] because UV absorption by LAI in the snow photic zone are at least
618 five orders of magnitude higher in Utah compared to Antarctica and Greenland.
619
620 In the snowpits following the fresh snowfall event, the existence of the dusty layer deeper
621 into the snow influences the vertical actinic flux profile and increases the photic zone
622 depth from 5 to 7 cm. The fresh snow at the surface contains less LAI compared to the
623 dusty layer, therefore actinic flux values are higher in the top several centimeters of snow
624 compared to actinic flux values measured before the snowfall event even though r_e values
625 in the new snow are a factor of 3.3-8.3 times smaller than the underlying depth hoar
626 grains. Smaller r_e values lead to more scattering in the snow, which increases the
627 probability of absorption by LAI. Although actinic flux values are highest at the surface
628 on January 31, Figure 4b illustrates that UV radiation is rapidly attenuated below the
629 fresh snow layer because radiation is forward-scattered into the highly-absorbing dusty
630 layer. As a result, there is roughly an order of magnitude less actinic flux at 14-cm depth
631 on January 31 compared to January 22.
632
633 The presence of a new dusty layer on the snow surface five days after the fresh snowfall
634 event does not significantly alter the vertical profile of normalized UV actinic flux likely
635 because UV absorption by LAI in the surface layer is at least 5 times lower than UV
636 absorption by LAI in the original dusty layer (surface snow from January 22 snowpit).

637 Surface snow UV albedo is strongly influenced by the presence of LAI, and
638 Supplemental Figure 2B shows that snow UV albedo is lowest right before the snowfall
639 event on January 30-31 and highest immediately afterwards.
640
641 We use these actinic flux profiles and the observed snow nitrate concentrations (Figure
642 3a-c) to calculate daily-averaged fluxes of snow-sourced N_r (molec cm^{-2} s^{-1}) at 1-cm
643 depth (z) increments in the snow ($F_{Nr}(z)$) and total fluxes of N_r to the boundary layer
644 (F_{Nr}) according to E8 and E9 for each of the three snowpits (Figure 4d-f). Prior to the
645 fresh snowfall event, $F_{Nr}(z)$ decreases exponentially with depth in the photic zone. $F_{Nr}(z)$
646 is highest at the snow surface because that is where both actinic flux and snow nitrate
647 concentrations are highest. Daily-average F_{Nr} summed over the snow photic zone is
648 5.6×10^8 molec cm^{-2} s^{-1} on January 22 (Figure 4d and Table 1). Immediately following the
649 fresh snowfall event, $F_{Nr}(z)$ decreases by a factor of 3 at the surface because of the factor
650 of 4 decrease in surface snow nitrate concentrations, which is partially compensated by
651 the higher UV actinic flux in the top of the snow photic zone (Figure 4b). The daily-
652 averaged F_{Nr} on January 31 is 1.9×10^8 molec cm^{-2} s^{-1}, which is a factor of 3 lower than
653 total F_{Nr} on January 22. Five days later, $F_{Nr}(z)$ has increased by a factor of 2 at the
654 surface due to the factor of 2 increase in surface nitrate concentrations (Figure 3c and 4f).
655 The daily-averaged F_{Nr} on February 4 is 3.2×10^8 molec cm^{-2} s^{-1}, which is a factor of 1.7
656 higher than total F_{Nr} on January 31.
657
658 **3.2.2. Snow Photochemistry Column Model**

659 The snow chemistry column model is used to calculate the time-dependent flux of snow-
660 sourced N_r (F_{Nr}) and the depth profile of nitrate concentration and $\delta^{15}N(NO_3^-)$. Figure 5
661 shows the diurnal F_{Nr} values on January 22, January 31, and February 4. The daily-
662 averaged snow F_{Nr} on January 22 is 6.3×10^8 molec cm^{-2} s^{-1}. Immediately following the
663 snow event, the daily-averaged snow F_{Nr} decreases by a factor of 11 compared to January
664 22 (5.6×10^7 molec cm^{-2} s^{-1}). The dramatic difference in F_{Nr} is due to the differences in
665 nitrate concentrations in the top several centimeters of snow. Modeled snow nitrate
666 concentrations in the fresh snow layer on January 31 are between 30 and 300 times lower
667 compared to nitrate concentrations in the dusty layer. Five days after the snow event, the
668 daily-averaged snow F_{Nr} has increased by a factor of 2 (1.2×10^8 molec cm^{-2} s^{-1}) because
669 deposition of nitrate to the snow surface layer enhances surface nitrate concentrations and
670 thus F_{Nr}. Calculated daily average F_{Nr} using observed (section 3.2.1) and modeled
671 (TRANSITS) snow nitrate concentrations agree within a factor of ~2 (Table 1); modeled
672 F_{Nr} tends to be lower because modeled snow nitrate concentrations are lower than
673 observed (Figure 3).
674
675 Figure 6 shows hourly F_{Nr} values calculated for the entire UBWOS2014 campaign using
676 TRANSITS. From the start of the campaign until the fresh snow event on January 31, the
677 daily maximum F_{Nr} values increase as surface snow nitrate concentrations increase due to
678 continual dry-deposition of atmospheric nitrate to the snow surface. Immediately after the
679 snow event on January 31, daily maximum F_{Nr} values are lowered by more than a factor
680 of 10 due to decreased nitrate concentrations in the snow photic zone. Following the
681 snow event, the flux of snow-sourced N_r gradually increases again due to dry-deposition

682 of nitrate to the surface layer, although daily maximum F_{Nr} values remain lower
683 compared to values before the snow event throughout the remainder of the field
684 campaign.
685
686 Figure 3 shows modeled snow nitrate concentrations and $\delta^{15}N(NO_3^-)$ from TRANSITS
687 compared to the observations. The general shapes of the modeled and measured vertical
688 profiles of nitrate concentration are in agreement for all three snowpits; both modeled and
689 measured nitrate concentrations are highest in the dusty layer and lowest near the bottom
690 of the snowpit (Figure 3a-c). Both the model and the observations show increased snow
691 nitrate concentrations at the surface following the fresh snowfall event, but the model
692 tends to underestimate surface snow nitrate concentrations after the snow event.
693
694 Modeled $\delta^{15}N(NO_3^-)$ is also within the range of observations (Figure 3d-f). Modeled
695 $\delta^{15}N(NO_3^-)$ at the top surface snow layer becomes more depleted from the January 22 to
696 the January 31 snowpit reflecting the decrease in atmospheric $\delta^{15}N(NO_3^-)$ in the model
697 based on surface snow observations (Figure 1a). Without additional snowfall between
698 January 31 and February 4, surface snow $\delta^{15}N(NO_3^-)$ becomes more enriched in the
699 model over this time period because model atmospheric $\delta^{15}N(NO_3^-)$ becomes more
700 enriched (Figure 1a). In contrast, the observations retain this light $\delta^{15}N(NO_3^-)$ at a depth
701 of ~2 cm until the February 11 snowpit (see supplement A). The difference between
702 modeled and observed $\delta^{15}N(NO_3^-)$ at 2 cm depth after January 31 may be due to the
703 redistribution of surface snow by wind, and the fact that each snowpit was dug in a
704 slightly different location. Blowing snow will bury the surface snow with light

705 $\delta^{15}N(NO_3^-)$, and subsequent atmospheric deposition of more enriched $\delta^{15}N(NO_3^-)$ will
706 occur onto this new, wind-blown snow surface, retaining the light $\delta^{15}N(NO_3^-)$ at 2 cm
707 depth. In contrast to the observations, the model does not account for windblown
708 redistribution of snow, and calculates the time-evolution of nitrate concentration and
709 $\delta^{15}N(NO_3^-)$ gradients of a single snowpit.
710
711 To examine the sensitivity of snow nitrate to photolysis, we turn off photolysis of snow
712 nitrate in the model by setting $\phi = 0$. When snow nitrate photolysis is turned off, snow
713 nitrate concentrations change by less than 0.5% in all snowpits, resulting in relatively
714 little sensitivity of modeled snow nitrate concentration to snow photochemistry because
715 only this small fraction (< 0.5%) of nitrate is lost via photolysis at all depths. Despite the
716 large nitrogen isotope fractionation (ε = -88 to -35‰) resulting from the photolysis of
717 snow nitrate, the difference in modeled $\delta^{15}N(NO_3^-)$ when snow nitrate is turned on (ϕ =
718 4.6×10^{-3}) and off ($\phi = 0$) is small because of the very small fraction of nitrate photolyzed.
719
720 In another sensitivity study, we calculate the maximum possible F_{Nr} in the Uintah Basin
721 by increasing the value of ϕ until modeled snow $\delta^{15}N(NO_3^-)$ falls outside the full range of
722 observations. Above $\phi = 0.2$, there is significant disagreement (when the maximum
723 change in $\delta^{15}N(NO_3^-)$ is > 1σ of the mean $\delta^{15}N(NO_3^-)$ in all snowpits) between modeled
724 and measured $\delta^{15}N(NO_3^-)$ values. Using $\phi = 0.2$ results in more enriched $\delta^{15}N(NO_3^-)$ at
725 depth due to enhanced photolytic loss, and more depleted $\delta^{15}N(NO_3^-)$ at the snow surface
726 due to the deposition of isotopically light snow-sourced nitrate. Using $\phi = 0.2$ results in a

727 maximum possible F_{Nr} at least 45 times larger than when using ϕ = 4.6x10^{-3} for all
728 snowpits (see Table 1).
729
730
731 **4. Impact of Snow-Sourced N_r on the Boundary Layer Reactive Nitrogen Budget**
732
733 **4.1. NO_x**
734 We first assume that all N_r is NO_x and use F_{Nr} values calculated using the snow
735 photochemistry column model to estimate the impact of F_{NOx} on the NO_x budget in the
736 Uintah Basin. Using the best estimate for the quantum yield of nitrate photolysis
737 (ϕ=4.6x10^{-3}), the modeled daily-averaged flux of snow-sourced NO_x ranges from 5.6x10^{7}
738 to 7.2x10^{8} molec cm^{-2} s^{-1} and the maximum F_{Nr} value is 3.1x10^{9} molec cm^{-2} s^{-1} for the
739 entire campaign (Supplementary Table 4B). The top-down NO_x emission inventory for
740 oil, gas, and all other sources excluding the Bonanza power plant in Duchesne and Uintah
741 counties is 6.5x10^{6} kg NO_x yr^{-1} [*Ahmandov et al*., 2015]. The power plant is excluded
742 because its emissions occur above the boundary layer due to the plume's positive
743 buoyancy. Assuming a constant NO_x emission rate and using the area of Duchesne (8433
744 km^2) and Uintah counties (11658 km^2), the top-down NO_x emission estimate for the
745 Uintah and Duchesne counties is 1.2x10^{12} molec cm^{-2} s^{-1}. The emission of primary NO_x
746 in these two counties is thus at least 300 times higher than the estimated snow NO_x
747 emissions, implying that snow-sourced NO_x fluxes likely do not influence the NO_x
748 boundary layer budget in the highly-polluted Uintah Basin. If the upper limit of ϕ = 0.2 is
749 used, snow-sourced NO_x emissions are still at least 7 times smaller than primary NO_x

750 emissions. Although reactive nitrogen is likely being emitted from the snow into the
751 boundary layer, the snow-sourced NO_x signal is swamped by emissions from primary
752 anthropogenic sources in the Uintah Basin.
753
754 **4.2. HONO**
755 Only the major channel for snow nitrate photolysis (E1) is simulated in the TRANSITS
756 model, although nitrate can also photolyze via E2 and form both NO_x and HONO (E3-
757 E5). The surface snow pH ranged from 2-4 during the campaign (see Figure 3A in
758 Supplemental Material), which is low enough to enable direct volatilization of HONO
759 from the snow. We estimate the maximum possible influence of the snow-photolytic
760 source of boundary layer HONO by assuming that all snow-sourced N_r is in the form of
761 HONO. If we assume that the campaign-maximum F_{Nr} value (3.1×10^9 molec cm^{-2} s^{-1}) is
762 all HONO that escapes from the snow into the boundary layer, a boundary layer height of
763 50 m, and a lifetime of HONO of 18 minutes (at solar noon) [*Edwards et al*., 2013], snow
764 nitrate photolysis would contribute a maximum of 25 pptv of HONO to the boundary
765 layer at solar noon. The modeled and observed Uintah Basin boundary layer HONO
766 mixing ratios presented in Edwards et al. [2014] range from ~20 pptv at night to up to
767 150 pptv during the day, which suggests that the daytime fluxes of reactive nitrogen are
768 not a significant source of HONO to the boundary layer compared to other HONO
769 sources in the basin. Our estimated maximum HONO flux is comparable to snow-sourced
770 HONO fluxes measured at another polluted, mid-latitude location (Paris, France),
771 estimates of which ranged from $0.7\text{-}3.1 \times 10^{10}$ molec cm^{-2} s^{-1} (assuming a snow density of
772 0.36 g cm^{-3} and snow photic zone depth of 6 cm) [*Michoud et al*., 2015]. If the upper

773 limit of ϕ = 0.2 is used (campaign-maximum F_{Nr} =1.4x10^{11} molec cm^{-2} s^{-1}), the maximum
774 boundary layer HONO mixing ratio calculated using this approach is 1.1 ppbv at solar
775 noon, which would significantly impact boundary layer HONO mixing ratios in the
776 Uintah Basin. Given that HONO is thought to be only a minor fraction of total N_r emitted
777 from snow [*Beine et al*., 2008], we consider this to be an overestimate.
778
779 **5. Conclusions**
780 This study estimates the influence of snow nitrate photolysis on the boundary layer
781 reactive nitrogen (N_r) budget in the Uintah Basin, which is a region with heavy oil and
782 natural gas extraction processes. Observations of snow optical properties, including
783 ultraviolet (UV) light-absorbing impurities (e.g., black carbon, dust, organics), radiation
784 equivalent ice grain radii, and snow density from 12 snowpits measured during the
785 Uintah Basin Winter Ozone Study (UBWOS) 2014 are incorporated into a snowpack
786 radiative transfer model to calculate vertical profiles of UV actinic flux in 12 snowpits
787 dug during the campaign. The calculated UV actinic flux profiles along with
788 measurements of nitrate concentration are used to calculate snow-sourced N_r fluxes
789 associated with snow nitrate photolysis using both a simple equation (E8) and a more
790 complex snow photochemistry column model, which yield similar results. Snow nitrate
791 photolysis in the column model is constrained by 1-cm depth resolved observations of
792 $\delta^{15}N(NO_3^-)$ in the snowpits, which is highly sensitive to UV photolysis [*Erbland et al*.,
793 2015].
794

795 The daily-averaged flux snow-sourced N_r (F_{Nr}) to the boundary layer ranges from $5.6x10^7$
796 to $7.2x10^8$ molec cm^{-2} s^{-1} and the modeled campaign-maximum F_{Nr} is $3.1x10^9$ molec cm^{-2}
797 s^{-1}. The top-down emission estimate of primary NO_x in the Uintah and Duchesne counties
798 reported in Ahmadov et al. [2015] is at least 300 times higher than estimated snow NO_x
799 emissions, assuming that all N_r is emitted as NO_x. This suggests that snow-sourced NO_x
800 fluxes likely have little influence on the boundary layer NO_x budget in the highly-
801 polluted Uintah Basin. Assuming that all N_r is emitted as HONO also suggests that the
802 snow-sourced reactive nitrogen fluxes associated with snow nitrate photolysis do not
803 significantly contribute to boundary layer HONO mixing ratios in the Uintah Basin. The
804 relative importance of the flux of NO_x and HONO will influence the impact of the
805 recycling of N_r in snow on the chemistry of the boundary layer in snow-covered regions,
806 but is unknown. Knowledge of the chemical speciation of snow-source N_r is required for
807 a better understanding of the full impact of snow on local oxidant budgets. However, in
808 the Uintah Basin, we conclude that air quality models can safely neglect the recycling of
809 reactive nitrogen in snow when identifying the most effective strategies for reducing
810 wintertime ozone abundances.
811
812 **Acknowledgements**
813 We gratefully acknowledge support from 155 backers from www.experiment.com, NSF
814 PLR 1244817, PMEL contribution number 4468, and an EPA STAR fellowship to M.C.
815 Zatko. The Uintah Basin Winter Ozone Studies were a collaborative project led and
816 coordinated by the Utah Department of Environmental Quality (UDEQ) with support
817 from the Uintah Impact Mitigation Special Service District (UIMSSD), the Bureau of

Land Management (BLM), the Environmental Protection Agency (EPA), and Utah State University. The authors acknowledge the NOAA/ESRL Chemical Sciences Division and Questar Energy Products for site preparation and support. We thank Kristen Shultz, Jim Johnson, Drew Hamilton, and Derek Coffman for all of their help before, during, and after the field campaign. We would also like to thank Dean Hegg for advice on aerosol sampling, Angela Hong and Jennifer Murphy for helpful discussions about NO_y vertical gradients, and Chad Mangum for laboratory assistance at USU. We thank Sarah Doherty for the use of the ISSW spectrophotometer and Stephen Warren for graciously allowing M.C. Zatko to borrow snow sampling instruments and gear and providing comments about this work. We thank Jonathan Raff for helpful discussions about soil microbial activity as well as Joost de Gouw and Gail Tonnesen for useful discussions about boundary layer HONO. Finally, we thank Lyatt Jaeglé, Joel Thornton, and Thomas Grenfell for their helpful comments. Joel Savarino and Joseph Erbland have been partly supported by a grant from Labex OSUG@2020 (Investissements d'avenir – ANR10 LABX56) during the development of the TRANSITS model.

References

Ahmadov, R., McKeen, S., Trainer, M., Banta, R., Brewer, A., Brown, S., Edwards, P.M., de Gouw, J.A., Frost, G.J., Gilman, J., Helmig, D., Johnson, B., Karion, A., Koss, A., Langford, A., Lerner, B., Olson, J., Oltmans, S., Peischl, J., Petron, G., Pichugina, Y., Roberts, J.M., Ryerson, T., Schnell, R., Senff, C., Sweeney, C., Thompson, C., Veres, P.R., Warneke, C., Wild, R., Williams, E.J., Yuan, B., Zamora, R.: Understanding high wintertime O3 pollution events in an oil- and natural gas-producing region of the western US. *Atmos. Chem. Phys*., 15, 411-429, doi:10.5194/acp-15-411-2015, 2015.

Anastasio, C. and Chu, L.: Photochemistry of nitrous acid (HONO) and nitrous acidium ion (H_2ONO^+) in aqueous solution and ice. *Environ. Sci. Tech*., 43, 1108-1114, 2009.

Beine, H., Colussi, A.J., Amoroso, A., Esposito, G., Montagnoli, M., Hoffman, M.R.: HONO emissions from snow. *Environ. Res. Lett*., 3, 045005, 6, 2008.

Berhanu, T.A., Meusinger, C., Erbland, J., Jost, R., Bhattcharya, S. K., Johnson, M. S., Savarino, J.: Laboratory study of nitrate photolysis in Antarctic snow. II. Isotopic effects and wavelength dependence. J. Chem. Phys., 140, 244306, doi:10.1063/1.4882899, 2014.

Carter, W. P. L., Seinfeld. J.H.: Winter O3 formation and VOC incremental reactivities in the Upper Green River Basin of Wyoming. Atmos. Environ., 50, 255-266, doi:10.1016/j.atmosenv.2011.12.025, 2012.

Casciotti, K.L., Sigman, D.M., Hastings, M., Bohlke, J.K., Hilkert, A.: Measurement of the oxygen isotopic composition of nitrate in seawater and freshwater using the denitrifier method. *Anal. Chem*., 74, 4905-4912, 2002.

Chu, L., and Anastasio. C.: Quantum Yields of Hydroxyl Radicals and Nitrogen Dioxide from the Photolysis of Nitrate on Ice. *J. Phys. Chem*., 107, 9594-9602, 2003.

Crowley, J.N., Ammann, M., Cox, R.A., Hynes, R.G., Jenkin, M.E., Mellouki, A., Rossi, M.J., Troe, J., Wallington, T.J.: Evaluated kinetic and photochemical data for atmospheric chemistry: Volume V – heterogeneous reactions on solid surfaces. Atmos. Chem. Phys., 10, 9059-9223, doi:10.5194/acp-10-9059-2010, 2010.

Delmas, R., Serca, D., Jambert, C.: Global inventory of NO_x sources. *Nutr. Cycl. Agroecosys*., 48, 51-60, 1997.

Doherty, S. J., Warren, S. G., Grenfell, T. C., Clarke, A. D., and Brandt, R. E.: Light-absorbing impurities in Arctic snow. *Atmos. Chem. Phys*., 10, 11647-11680, doi:10.5194/acp-10-11647-2010, 2010.

Domine, F., Bock, J., Voisin, D., Donaldson, D. J.: Can we model snow photochemistry? Problems with the current approaches. *J. Phys. Chem. A*, 117, 4733-4749, doi: 10.1021/jp3123314 2013.

894 Durham, J.L., Stockburger, L.: Nitric acid-air diffusion coefficient: Experimental
895 determination. *Atmos. Environ*., 20(3), 559-563, 1986.
896
897 Edwards, P.M., Young, C.J., Aikin, K., de Gouw, J., Dube, W., Geiger, P., Gilman, J.,
898 Helmig, D., Holloway, J.S., Kercher, J., Lerner, B., Martin, R., McLaren, R., Parrish,
899 D.D., Peischl, J., Roberts, J.M., Ryerson, T.N., Thornton, J., Warneke, C., Williams, E.J.,
900 Brown, S.S.: O3 photochemistry in an oil and natural gas extraction region during winter:
901 simulations of a snow-free season in the Uintah Basin, Utah. *Atmos. Chem. Phys*., 13,
902 8955-8971, doi:10.5194/acp-13-8955-2013, 2013.
903
904 Edwards, P.M., Brown, S., Roberts, J., Ahmadov, R., Banta, R., de Gouw, J., Dube, W.,
905 Field, R., Flynn, J., Gilman, J., Graus, M., Helmig, D., Koss, A., Langford, A., Lefer, B.,
906 Lerner, B., Li, R., Li, S., McKeen, S., Murphy, S., Parrish, D., Senff, C., Soltis, J., Stutz,
907 J., Sweeney, C., Thompson, C., Trainer, M., Tsai, C., Veres, P., Washenfelder, R.,
908 Warneke, C., Wild, R., Young, C., Yuan, B., Zamora, R.: High O3 pollution from
909 carbonyl photolysis in an oil and gas basin. *Nature*, 514, 351-354,
910 doi:10.1038/nature13767, 2014.
911
912 Erbland, J., Savarino, J., Morin, S., France, J.L., Frey, M.M., King, M.D.: Air-snow
913 transfer of nitrate on the East Antarctic plateau – Part 2: An isotopic model for the
914 interpretation of deep ice-core records. *Atmos. Chem. Phys.*, 15, 12079-12113,
915 doi:10.5194/acpd-15-12079-2015, 2015.
916
917 Felix, J.D., Elliott, E.M., Shaw, S.L: Nitrogen isotopic composition of coal-fired power
918 plant NO_x: Influence of emissions controls and implications for global emission
919 inventories. *Env. Sci. Tech*., 46, 3528-3535, 2012.
920
921 Felix, J.D., Elliot, E.M.: Isotopic composition of passively collected nitrogen dioxide
922 emissions: Vehicle, soil and livestock source signatures. *Atmos. Environ*., 92, 359-366,
923 doi:10.1016/j.atmosenv.2014.04.005, 2014.
924
925 Field, R.A., Soltis, J., McCarthy, M.C., Murphy, S., Montague, D.C.: Influence of oil and
926 gas field operations on spatial and temporal distributions of atmospheric non-methane
927 hydrocarbons and their effect on O3 formation in winter. *Atmos. Chem. Phys*., 15, 3527-
928 3542, doi:10.5194/acp-15-3527-2015, 2015.
929
930 Frey, M. M., Savarino, J., Morin, S., Erbland, J., and Martins, J. M. F.: Photolysis imprint
931 in the nitrate stable isotope signal in snow and atmosphere of East Antarctica and
932 implications for reactive nitrogen cycling. *Atmos. Chem. Phys*., 9, 8681-8696, 2009.
933
934 Freyer, H.D., Kley, D., Volz-Thomas, A., Kobel, K.: On the interaction of isotopic
935 exchange processes with photochemical reactions in atmospheric oxides of nitrogen. *J.*
936 *Geophys. Res*., 98, D8, 14791-14786, doi: 10.1029/93JD00874, 1993.
937

938 Gilman, J.B., Lerner, B.M., Kuster, W.C., de Gouw, J.A.: Source signature of volatile
939 organic compounds from oil and natural gas operations in northeastern Colorado.
940 *Environ. Sci. Technol*., 47, 1297-1305, doi:10.1021/es304119a, 2013.
941
942 Grannas, A. M., Jones, A. E., Dibb, J., Ammann, M., Anastasio, C., Beine, H. J., Bergin,
943 M., Bottenheim, J., Boxe, C. S., Carver, G., Chen, G., Crawford, J. H., Domine, F., Frey,
944 M. M., Guzman, M. I., Heard, D. E., Helmig, D., Hoffman, M. R., Honrath, R. E., Huey,
945 L. G., Hutterli, M., Jacobi, H. W., Klan, P., Lefer, B., McConnell, J., Plane, J., Sander,
946 R., Savarino, J., Shepson, P. B., Simpson, W. R., Sodeau, J. R., von Glasow, R., Weller,
947 R., Wolff, E. W., Zhu, T.: An overview of snow photochemistry: evidence, mechanisms
948 and impacts. *Atmos. Chem. Phys*., 7, 4329-4373, 2007.
949
950 Grenfell, T. C.: A Radiative Transfer Model for Sea Ice With Vertical Structure
951 Variations. *J. Geophys. Res*., 96, 16991-17001, 1991.
952
953 Grenfell, T.C., Warren, S.G.: Representation of a nonspherical ice particle by a collection
954 of independent spheres for scattering and absorption of radiation. *J. Geophys. Res*.,
955 104(D24), 31697-31709, 1999.
956
957 Grenfell, T.C., Doherty, S.J., Clarke, A.D., Warren, S.G.: Light absorption from
958 particulate impurities in snow and ice determined by spectrophotometric analysis of
959 filters. Appl. Opt., 50(8), 2037-2048, doi:10.1364/AO.50.002037, 2011.
960
961 Guenther, A., Hewitt, N.C., Erickson, D., Fall, R., Geron, C., Graedel, T., Harley, P.,
962 Klinger, L., Lerdau, M., McKay, W.A., Pierce, T., Scholes, B., Steinbrecher, R.,
963 Tallamraju, R., Taylor, J., Zimmerman, P.: A global model of natural volatile organic
964 compound emissions. *J. Geophys. Res*., 100(D5), 8873-8892, 1995.
965
966 Hansen, J.E., Travis, L.D.: Light scattering in planetary atmospheres. *Space. Sci. Rev*.,
967 16, 527-610, 1974.
968
969 Heaton, T. H. E., Spiro, B., Robertson, M.C., *Oecologia*, 109, 4, 600-607, 1997.
970
971 Helmig, D., Thompson, C.R., Evans, J., Boylan, P., Hueber, J., Park, J.H.: Highly
972 elevated atmospheric levels of volatile organic compounds in the Uintah Basin, Utah.
973 *Environ. Sci. Technol*., 48, 4707-4715, doi:10.1021/es405046r, 2014.
974
975 Honrath, R.E., Guo, S., Peterson, M.C., Dziobak, M.P., Dibb, J.E., Arsenault, M.A.:
976 Photochemical production of gas phase NO_x from ice crystal NO_3^-. *J. Geophys. Res*.,
977 105(D19), 24183-24190, 2000.
978
979 Kaiser, J., Hastings, M.G., Houlton, B.Z., Rockmann, T., Sigman, D.M.: Triple oxygen
980 isotope analysis of nitrate using the denitrifier method and thermal decomposition of
981 N_2O. *Anal. Chem*., 79, 599-607, doi:10.1021/ac061022s, 2007.
982

Logan, J.A., Nitrogen oxides in the troposphere: Global and regional budgets. *J. Geophys. Res*., 88(C15), 10785-10807, doi:10.1029/JC088iC15p10785, 1983.

Mack, J., and Bolton, J. R.: Photochemistry of nitrite and nitrate in aqueous solution: A review. *J. Photochem. Photobiol*. A., 128, 1-13, 1999.

Martin, R., Moore, K., Mansfield, M., Hill, S., Harper, K., Shorthill, H.: Final report: Uintah Basin winter O3 and air quality study, December 2010 – March 2011. Energy Dynamics Laboratory, document number: EDL/11-039, 2011.

Massman, W.J. A review of the molecular diffusivities of H_2O, CO_2, CH_3, CO, O_3, SO_2, NH_3, N_2O, NO, and NO_2 in air, O_2 and N_2 near STP. *Atmos. Environ*., 32(6), 1111-1127, doi:10.1016/S1352-230(97)00391-9, 1998.

Markvart, T., Castalzer, L.: Practical handbook of photovoltaics: fundamentals and applications. Elsevier. ISBN 1-85617-390-9, 2003.

Matthias, A.D., Fimbres, A., Sano, E.E., Post, D.F., Accioly, L., Batchily, A.K., Ferreira, L.G.: Surface roughness effects on soil albedo. *Soil Sci. Soc. Am*. J., 64, 1035-1041, 2000.

Meusinger, C., Berhanu, T.A., Erbland, J., Savarino, J., Johnson, M.S.: Laboratory study of nitrate photolysis in Antarctic snow. I. Observed quantum yield, domain of photolysis, and secondary chemistry. *J. Chem. Phys*., 140, 244305, doi:10.1063/1.4882898, 2014.

Michoud, V., Doussin, Jean-Francois, Colomb, A., Afif, C., Borbon, A., Camredon, M., Aumont, B., Legrand, M., Beekman, M.: Strong HONO formation in a suburban site during snowy days. *Atmos. Environ*., 116, 155-158, doi:10.1016/j.atmosenv.2015.06.040, 2015.

Morin, S., Savarino, J., Frey, M.M., Domine, F., Jacobi, H.-W., Kaleschke, L., Martins, J.M.F.: Comprehensive isotopic composition of atmospheric nitrate in the Atlantic Ocean boundary layer from 65°S to 79°N. *J. Geophys. Res*., 114, D05303, doi:10.1029/208JD010696, 2009.

Oltmans, S.J., Schnell, R.C., Johnson, B.J., Petron, G., Mefford, T., Neely III, R.: Anatomy of wintertime O3 production associated with oil and gas extraction activity in Wyoming and Utah. *Elem. Sci. Anth*., 2, 000024, doi:10.12952/journal.elementa.000024, 2014.

Quinn, P.K., Coffman, D.J., Kapustin, V.N., Bates, T.S., Covert, D.S.: Aerosol optical properties in the MBL during ACE-1 and the underlying chemical and physical aerosol properties. J. Geophys. Res., 103, 16547-16564, 1998.

Quinn, P.K., Bates, T.S., Miller, T.L., Coffman, D.J., Johnson, J.E., Harris, J.M., Ogren, A., Forbes, G., Anderson, T.L., Covert, D.S., Rood, M.J.: Surface submicron aerosol

chemical composition: what fraction is not sulfate? *J. Geophys. Res*., 105(D5), 6785-6805, doi:10.1029/1999JD901034, 2000.

Rappengluck, B., Ackermann, L., Alvarez, S., Golovko, J., Buhr, M., Field, R.A., Soltis, J., Montague, D.C., Hauze, B., Adamson, S., Risch, D., Wilkerson, G., Bush, D., Stoekenius, T., Keslar, C.: Strong wintertime O3 events in the Upper Green River basin, Wyoming. *Atmos. Chem. Phys*., 14, 4909-4934, doi.10.5194/acp-14-4909-2014, 2014.

Rolph, G.D.: Real-time Environmental Applications and Display sYstem (READY) Website (http://www.ready.noaa.gov). NOAA Air Resources Laboratory, College Park, MD, 2016.

Schnell, R.C., Oltmans, S.J., Neely, R.R., Endres, M.S., Molenar, J.V., White, A.B.: Rapid photochemical production of O3 at high concentrations in a rural site during winter. *Nat. Geosci*., 2, 120-122, doi:10.1038/ngeo415, 2009.

Sigman, D.M., Casciotti, K.L., Andreani, M., Barford, C., Galanter, M., Bohlke, J.K.: A bacterial method for the nitrogen isotopic analysis of nitrate in seawater and freshwater. *Anal. Chem*., 73, 4145-4153, doi:10.1021/ac010088e, 2001.

Silva, S.R., Kendall, C., Wilkinson, D.H., Ziegler, A.C., Chang, C.C.Y., Avanzino, R.J.: A new method for collection of nitrate from fresh water and analysis of the nitrogen and oxygen isotope ratios. *J. Hydrol*., 228, 22-36, 2000.

Stamnes, K., Tsay, S., Wiscombe, W., Jayaweera, K.: Numerically stable algorithm for discrete-ordinate-method radiative transfer in multiple scattering and emitting layered media. *Appl. Opt*., 27, 2502-2509, 1988.

Stein, A.F., Draxler, R.R, Rolph, G.D., Stunder, B.J.B., Cohen, M.D., and Ngan, F.:. NOAA's HYSPLIT atmospheric transport and dispersion modeling system, *Bull. Amer. Meteor. Soc*., 96, 2059-2077, 2015, http://dx.doi.org/10.1175/BAMS-D-14-00110.1

Thompson, A.M., The oxidizing capacity of the Earth's atmosphere: Probable past and future changes. *Science*, 256, 1157-1165, 1992.

US EIA (US Energy Information Administration): Annual energy outlook 2014 Early Release Overview, Office of Integrated and International Energy Analysis US Department of Energy, Washington, DC 20585, available at: http://www.eia.gov/forecasts/aeo/er/pdf/0383er(2014).pdf (last access 24 March 2015), Report, 2014.

Veres, P.R., Roberts, J.M., Wild, R.J., Edwards, P.M., Brown, S.S., Bates, T.S., Quinn, P.K., Johnson, J.E., Zamora, R.J., de Gouw, J.: Peroxynitric acid (HO_2NO_2) measurements during the UBWOS 2013 and 2014 studies using iodide ion chemical ionization mass spectrometry. *Atmos. Chem. Phys*., 15, 8101-8114, doi:10.5194/acp-15-8101-2015, 2015.

Warneke, C., Geiger, F., Edwards, P.M., Dube, W., Petron, G., Kofler, J., Zahn, A., Brown, S.S., Graus, M., Gilman, J.B., Lerner, B.M., Peischl, J., Ryerson, T.B., de Gouw, J.A., Roberts, J.M.: Volatile organic compound emissions from the oil and natural gas industry in the Uintah Basin, Utah: oil and gas well pad emissions compared to ambient air composition. *Atmos. Chem. Phys*., 14, 10977-10988, doi:10.5194/acp-14-10977-2014, 2014.

Warren, S.G., Brandt, R.E., Grenfell, T.C.: Visible and near-ultraviolet absorption spectrum of ice from transmission of solar radiation into snow. *Appl. Opt*., 45, 21, 2006.

Walters, W.W., Goodwin, S.R., Michalski, G.: Nitrogen stable isotope composition $\delta^{15}N$ of vehicle-emitted NO_x. *Environ. Sci. Tech*., 49, 2278-2285, doi:10.1021/es505580v, 2015.

Walters, W.W., Michalski, G.:Theoretical calculation of nitrogen isotope equilibrium exchange fractionation factors for various NO_y molecules. *Geochem. Cosmochem. Acta*., 164, 284-297, doi:10.1016/j.gca.2015.05.029, 2015.

Walters, W.W., Simonini, D.S., Michalski, G.: Nitrogen isotope exchange between NO and NO_2 and its implications for $\delta^{15}N$ variations in tropospheric NO_x and atmospheric nitrate. *Geophys. Res. Lett*., 43, 1, 440-448, 10.1002/2015Gl066438, 2016.

Wild, R.J., Edwards, P.M., Bates, T.S., Cohen, R.C., deGouw, J.A., Dube, W.P., Gilman, J.B., Holloway, J., Kercher, J., Koss, A.R., Lee, L., Lerner, B.M., McLaren, R., Quinn, P.K., Roberts, J.M., Stutz, J., Thornton, J.A., Veres, P.R., Warneke, C., Williams, E., Young, C.J., Yuan, B., Zarzana, K.J., Brown, S.S.: Reactive nitrogen partitioning and its relationship to winter ozone events in Utah. *Atmos. Chem. Phys*., 16, 573-583, doi:10.5194/acp-16-573-2016, 2016.

Wiscombe, W.J.: The delta-M method: Rapid yet accurate radiative flux calculations for strongly asymmetric phase functions. *J. Atmos. Sci*., 34, 1408-1422, 1977.

Yuan, B., Liggio, J., Wentzell, J., Li, S. M., Stark, H., Roberts, J. M., Gilman, J., Lerner, B., Warneke, C., Li, R., Leithead, A., Osthoff, H. D., Wild, R., Brown, S. S., and de Gouw, J. A.: Secondary formation of nitrated phenols: insights from observations during the Uintah Basin Winter Ozone Study (UBWOS) 2014, *Atmos. Chem. Phys*., 16, 2139-2153, 10.5194/acpd-16-2139-2016, 2016.

Zatko, M.C., Grenfell, T.C., Alexander, B., Doherty, S.J., Thomas, J.L., Yang, X., The influence of snow grain size and impurities on the vertical profiles of actinic flux and associated NO_X emissions on the Antarctic and Greenland ice sheets. *Atmos*. *Chem*. *Phys*., 13, 3547-3567, doi:10.5194/acp-13-3547-2013, 2013.

Zatko, M.C. and Warren, S.G.: East Antarctic sea ice in spring: spectral albedo of snow, nilas, frost flowers, and slush; and light-absorbing impurities in snow. *Ann. Glaciol.*

Special Issue: Sea ice in a changing environment, 56(69), doi:10.3189/2015AoG69A574, 2015.

Zatko, M.C., Geng, L., Alexander, B., Sofen, E., Klein, K.: The impact of snow nitrate photolysis on boundary layer chemistry and the recycling and redistribution of reactive nitrogen across Antarctica and Greenland in a global chemical transport model. *Atmos. Chem. Phys*., 16, 2819-2842, doi:10.5194/acp-16-2819-2016, 2016.

Zhou, X., Beine, H.J., Honrath, R.E., Fuentes, J.D., Simpson, W., Shepson, P.B., Bottenheim, J.W.: Snowpack photochemical production of HONO: a major source of OH in the Arctic boundary layer in springtime. *Geophys. Res. Lett*., 28(21), 4087-4090, 2001.

Zhu, C., Xiang, B., Chu, L.T., Zhu, L.: 308 nm Photolysis of Nitric Acid in the Gas Phase, on Aluminum Surfaces, and on Ice Films. *J. Phys. Chem. A*., 114, 2561-2568, doi: 10.1021/jp909867a, 2010.

Table 1. Snow photic zone depth and daily-averaged modeled F_{Nr} calculated using E8 and the TRANSITS model on January 22, January 31, and February 4.

Pit Date	Photic zone depth (cm)	Daily-averaged F_{Nr} (molec cm^{-2} s^{-1})		
		E8	TRANSITS ($\phi = 4.6 \times 10^{-3}$)	TRANSITS ($\phi = 0.2$)
January 22	5.0	5.6×10^{8}	6.3×10^{8}	2.9×10^{10}
January 31	7.0	1.9×10^{8}	5.6×10^{7}	2.7×10^{9}
February 4	7.0	3.2×10^{8}	1.2×10^{8}	5.6×10^{9}

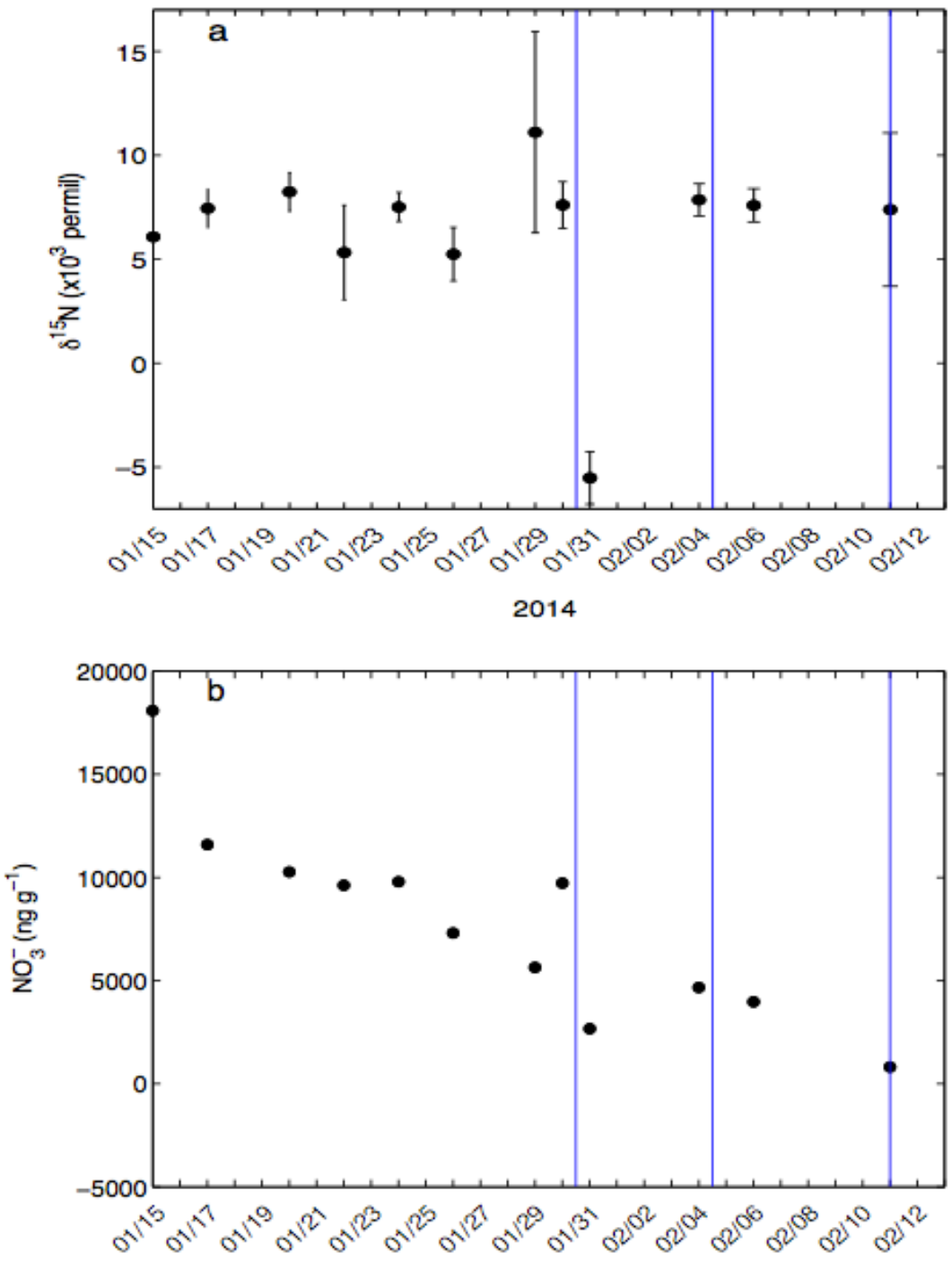

Figure 1. (a) Mean surface snow (top 1 cm) $\delta^{15}N(NO_3^-)$ observations (‰) for triplicate measurements from each snowpit (close circles). The full range of triplicate measured surface snow $\delta^{15}N(NO_3^-)$ for each snowpit is also indicated (vertical black lines). (b) Surface snow nitrate concentration measurements (ng g^{-1}) for each snowpit. The uncertainty in the concentration measurements is 0.75‰. The vertical blue lines indicate snowfall events.

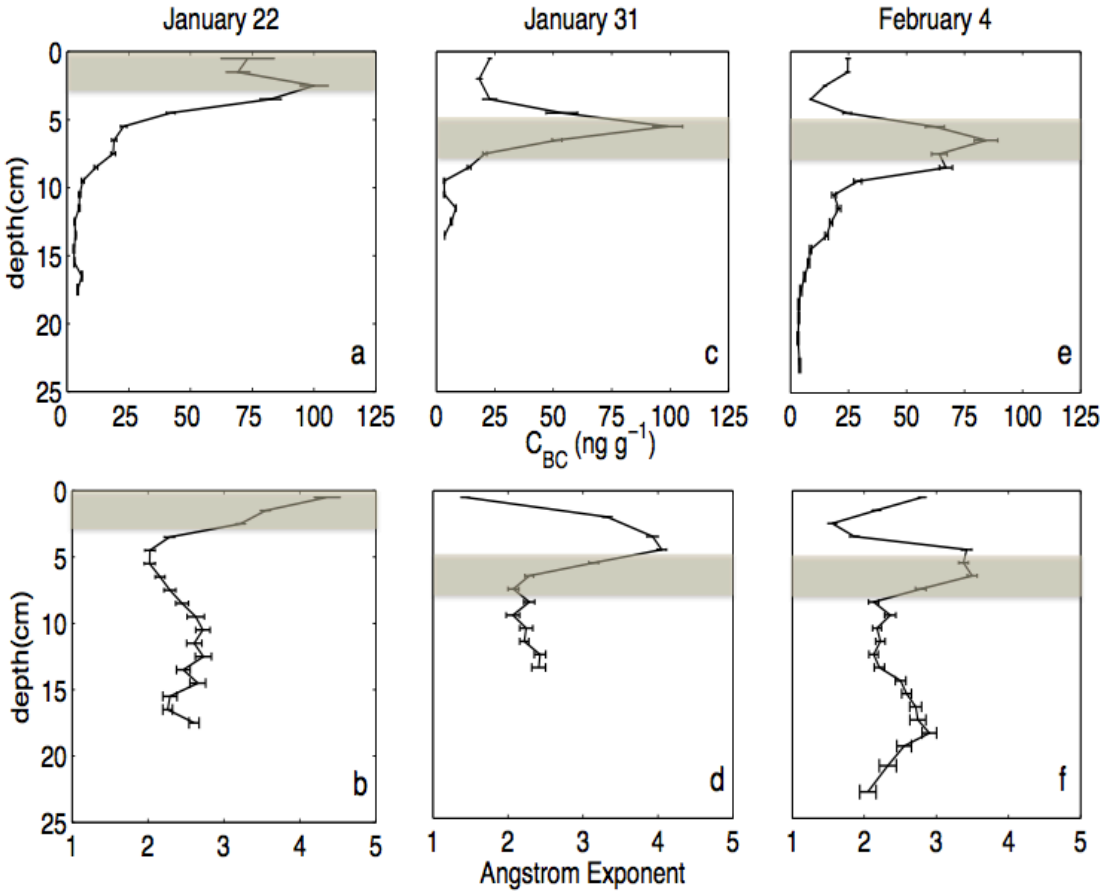

Figure 2. Snow optical properties measured on January 22 (top), January 31 (middle), and February 4 (bottom). (top) Vertical profiles of mean snow black carbon (C_{BC}, ng g^{-1}) measurements and the full range of C_{BC} measured at each depth (horizontal black lines), (bottom) mean Ångstrom exponent (Å, unitless) measurements and the full range of Å measured at each depth (horizontal black lines). The brown shaded region represents the dusty layer as defined in the text.

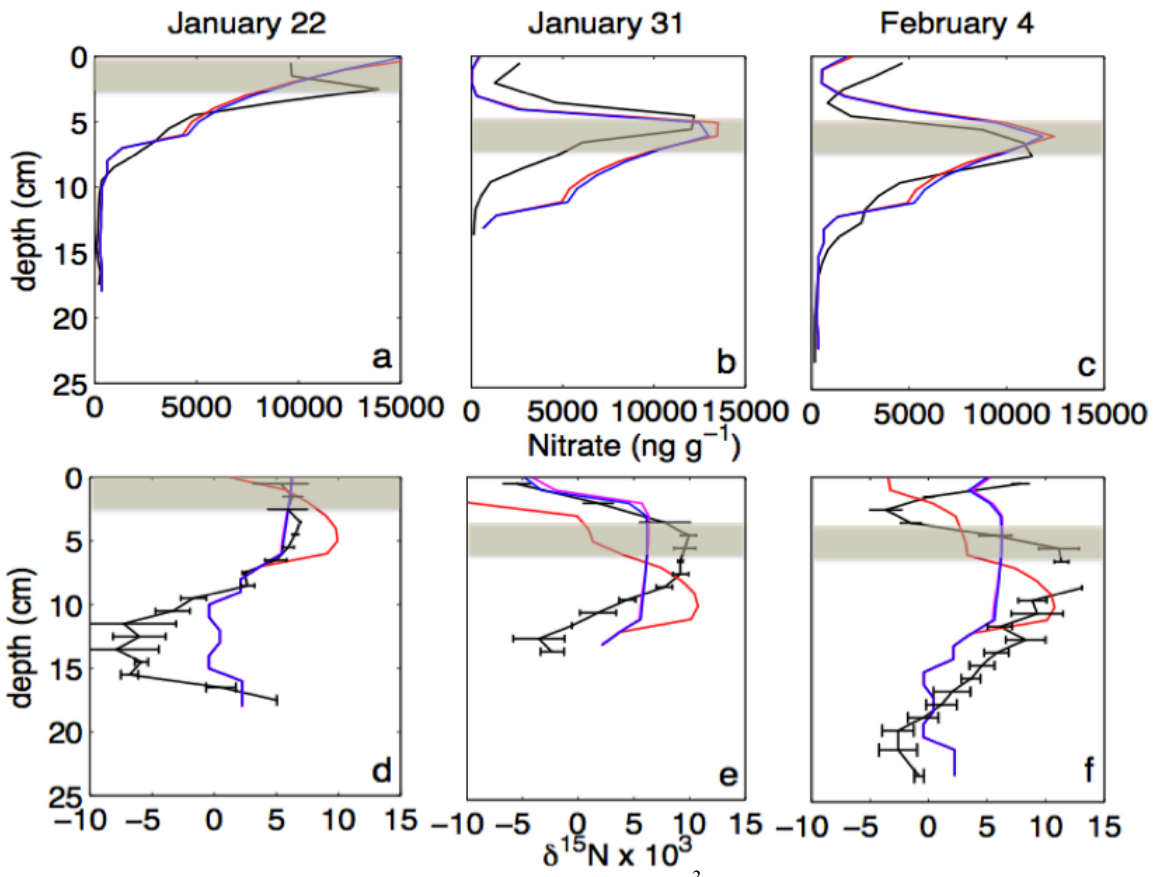

Figure 3. Measured (black) and modeled (Φ=4.6x10^{-3}, blue; Φ=0.2, red) vertical profiles of snow nitrate concentration (top) and $\delta^{15}N(NO_3^-)$ (bottom) on January 22 (left), January 31 (center), and February 4 (right). Modeled $\delta^{15}N(NO_3^-)$ profiles are calculated using variable quantum yields (Φ=4.6x10^{-3}, blue; Φ=0.2, red, Φ=0, magenta). The brown shaded region represents the dusty layer.

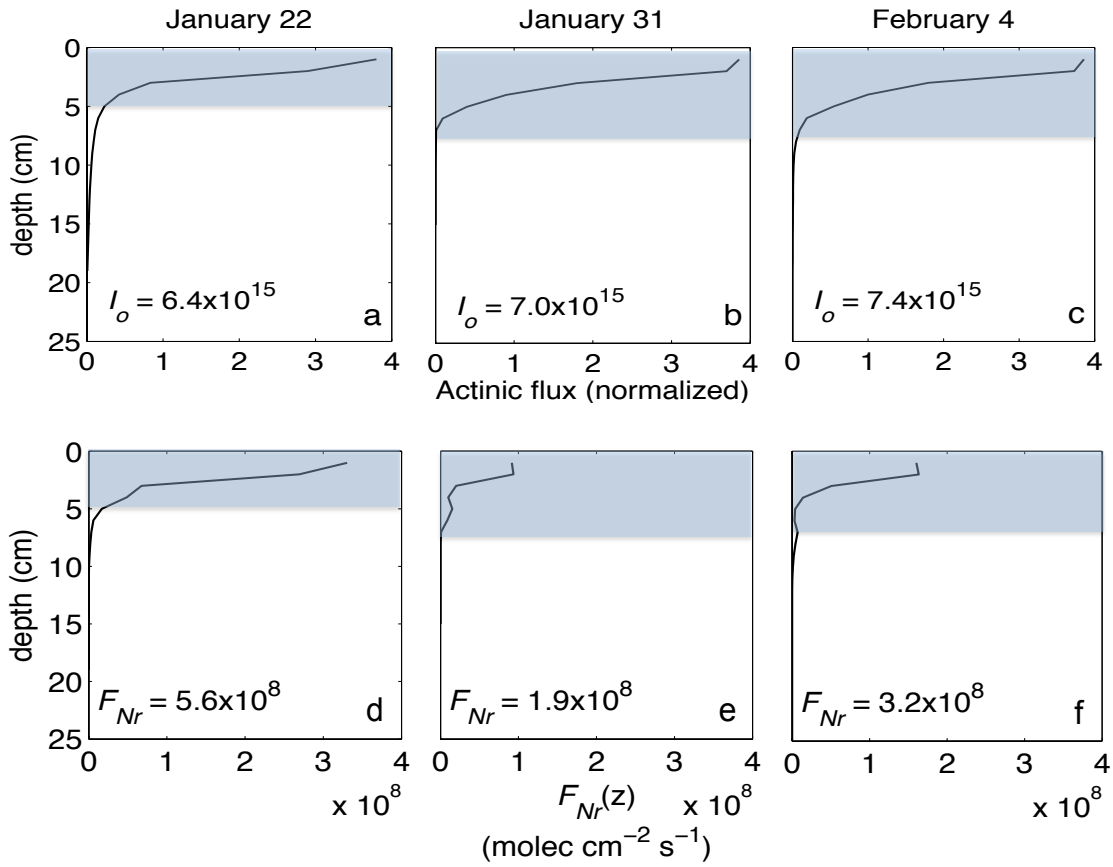

Figure 4. (a-c) Modeled vertical profiles of UV actinic flux (I, photons cm^{-2} s^{-1}) normalized to surface downwelling irradiance (I_o, photons cm^{-2} s^{-1}). Also presented is measured total UV I_o (λ=300-350 nm) for a solar zenith angle of 60° on each day. (d-f) Modeled vertical profiles of snow-sourced N_r fluxes (F_{Nr}, molec cm^{-2} s^{-1}) calculated using E8. Also shown is total F_{Nr}, which is the depth-integrated F_{Nr} over the photic zone. The blue shaded region represents the snow photic zone.

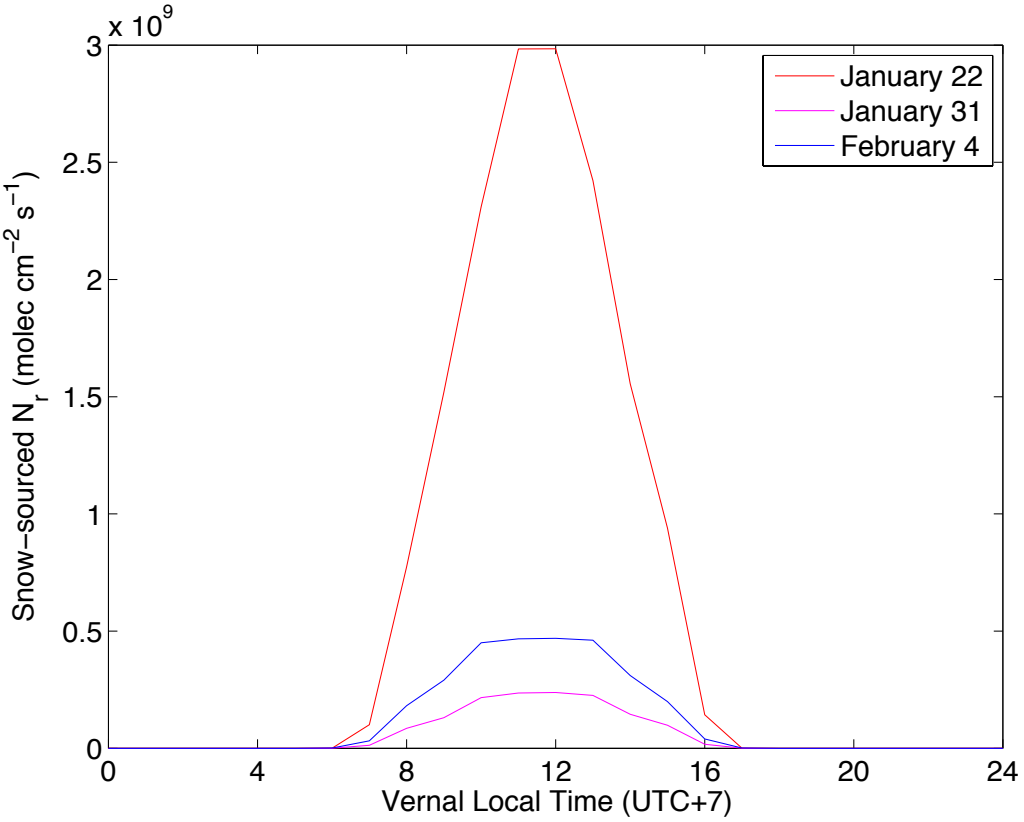

Figure 5. Modeled diurnal profiles of snow-sourced N_r fluxes (F_{Nr}, molec cm^{-2} s^{-1}) calculated using TRANSITS on January 22 (red), January 31 (magenta), and February 4 (blue).

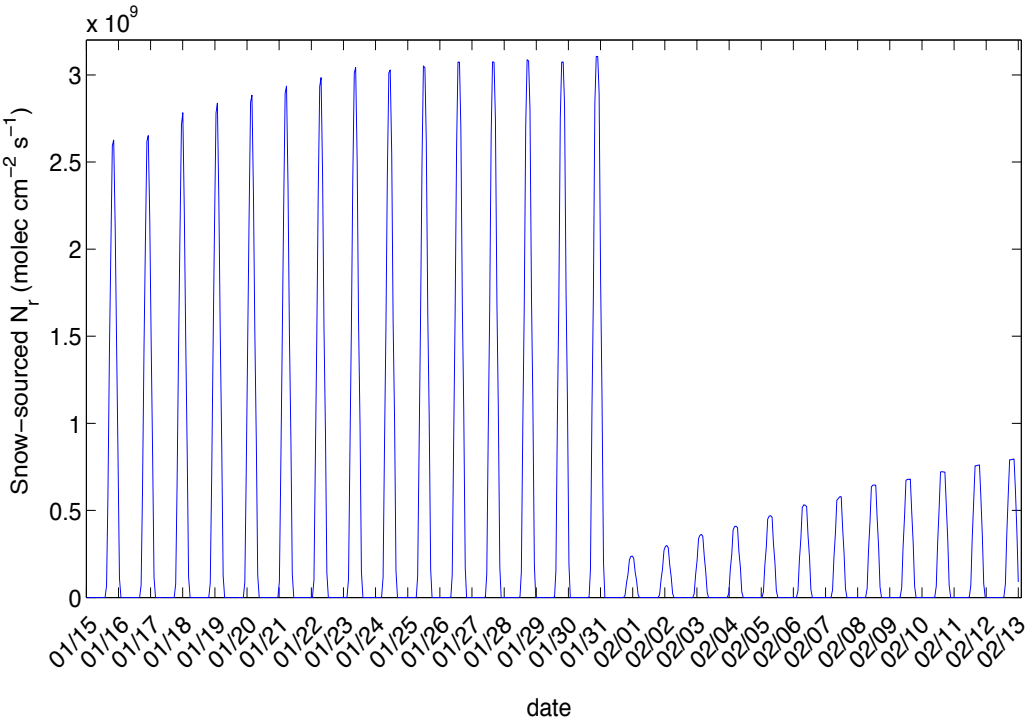

Figure 6. Modeled snow-sourced N_r fluxes (molec cm^{-2} s^{-1}) for each hour during the campaign from January 15 to February 11.